Available online at www.sciencedirect.com
ScienceDirect
Comput. Methods Appl. Mech. Engrg. 354 (2019) 593–619
Computer methods in applied mechanics and engineering
www.elsevier.com/locate/cma

Topology optimization of functionally-graded lattice structures with buckling constraints

Bing Yi[a,b,*], Yuqing Zhou[b], Gil Ho Yoon[c,b], Kazuhiro Saitou[b]

[a] School of Traffic and Transportation Engineering, Central South University, China
[b] Department of Mechanical Engineering, University of Michigan, USA
[c] School of Mechanical Engineering, Hanyang University, Republic of Korea

Received 27 February 2019; received in revised form 31 May 2019; accepted 31 May 2019
Available online 12 June 2019

Highlights

- A new method for topology optimization of functionally-graded lattice structure.
- The buckling constraint is employed to improve the stability of infill lattice.
- The method achieves high spatial lattice variations with guaranteed smooth connectivity.
- The method generate stiff structure comparable to SIMP and with level of structural stability.

Abstract

Lattice structures have been widely studied due to their advantage of low stiffness-to-weight ratio or sometimes auxetic properties. This paper presents a topology optimization method for structures with functionally-graded infill lattices with buckling constraints, which minimizes compliance while ensuring a prescribed level of structural stability against buckling failures. To realize topologically-optimized structures filled with functionally-graded lattices, Helmholtz PDE-filter with a variable radius is applied on the density field in Solid Isotropic Material with Penalization (SIMP) method. Buckling load factors based on the linear buckling analysis is employed as buckling constraints. Numerical examples show that proposed method can generate stiff structures comparable to the ones by the SIMP, with functionally-graded infill lattices that improve the structural stability by avoiding long, slender features under compression.

Keywords: Variable infill; Lattice structure; Topology optimization; Linear buckling

1. Introduction

Nature has the ability of creating lattice structures to improve mechanical properties with low density. Common natural lattice structures are honeycomb (woods and corks), parenchyma in plant (corns), and sponges (spongy bones and sea sponges) [1], which exhibits superior mechanical properties such as high stiffness-to-weight ratio, robustness against unknown loads, and auxetic property. Inspired by these lattice structures in nature, many

* Corresponding author at: School of Traffic and Transportation Engineering, Central South University, China.
E-mail address: bingyi@csu.edu.cn (B. Yi).

https://doi.org/10.1016/j.cma.2019.05.055
0045-7825/

Table 1
Summary of previous work.

		Length scales for material models	
		Single-scale	Bi-scale
Steps required to obtain output designs	One step	Bendsøe & Kikuchi [17], Liu et al. [19], Wu et al. [20] Wu et al. [21], Träff et al. [22]	Coelho et al. [23], Chen et al. [24], Wang et al. [25], Wang et al. [26], Panesar et al. [27], Radman et al. [28], Daynes et al. [29], Li et al. [30], Deng et al. [31], Xu et al. [32], Wang et al. [33], Nishi et al. [34], Campagna et al. [35], Du et al. [36]
	Two step	Pantz et al. [37], Groen et al. [38], Grégoire et al. [39]	Panetta et al. [40], Zhu et al. [41], Takano et al. [42], Liang et al. [43]

engineered lattice structures are widely utilized in structural components with high stiffness–density ratio [2,3], high energy-absorbing capability [4,5], negative Poison's ratio [6–8], extreme thermal expansion [9–11], and special acoustic properties [12–14]. Thanks to the development of additive manufacturing, which fully leverages the geometric versatility of layer-upon-layer additive processes, the design, fabrication, and validation of engineered lattice structures have become active research topics [15,16]. Due to its affinity with additive manufacturing, it is just natural that topology optimization [17,18] has emerged as the foundation for optimally designing engineered lattice structures.

Existing approaches for designing functionally-graded lattice structures based on topology optimization can be classified according to two criteria: the number of length scales for material models (single- or bi-scale methods) and the number of steps required to obtain the output designs (one- and two-step optimization). Table 1 summarizes the previous works in each category, which are discussed further in Section 2. These approaches have been proposed in the pursuit of realizing the lattice structures that are functionally highly graded as well as structurally well connected, which often conflict with each other.

This paper presents a new method for the topology optimization of functionally-graded lattice structures, which achieves high spatial lattice variations with guaranteed connectivity. It minimizes structural compliance subject to buckling constraints, which ensure a prescribed level of structural stability against buckling failures. The novelty of the proposed method is two-fold: it realizes designs with (1) fully-connected, functionally-graded lattices by the variable-radius Helmholtz PDE-filter applied on the density field in Solid Isotropic Material with Penalization (SIMP) method, and (2) a prescribed level of buckling safety, by explicitly employing constraints on buckling load factors based on the linear buckling analysis.

The remainder of this paper is organized as follows. Section 2 discusses the review of related literature. Section 3 describes the definitions of design fields: material density and averaging radius, the optimization model, and the sensitivities of the objective and constraints with respect to the design fields. The numerical examples for compliance minimization subject to buckling constraints are given in Section 4. Finally, the conclusion and future work are presented in Section 5.

2. Literature review

2.1. Single-scale methods

The first-reported work on topology optimization by Bendsøe and Kikuchi [17] using the material homogenization of parameterized lattice cells can be seen as the origin of the single-scale, one-step methods. However, the obtained results were never interpreted as lattice structures since there was no manufacturing process back then that could fabricate them. Liu et al. [19] extended the moving morphable component method to design functionally-graded lattice structures. Although it can optimize a lattice structure in a single step, it is highly sensitive to the initialization. Wu et al. [20] proposed a simple but effective method to produce beak-like lattice structures by adopting a local volume constraint for SIMP. Following this work, Wu et al. [21] proposed the shell-infill composite topology optimization method. Träff et al. [22] also proposed a single scale microstructure optimization method by

using a mapping approach. While these work demonstrated that the buckling property can be improved in the resulting designs, it is not explicitly considered during optimization.

A few papers have reported single-scale, two step methods as the post-processing of the results of homogenization-based topology optimization. Pantz [37] first macroscopically project the microstructure of the optimal result from homogenization method to a workable shape. Groen [38] and Grégoire [39] proposed a projection method and a conformal mapping method, respectively, to optimize the orientations of lattice cells to improve the material connectivity in the design domain and in turn to improve manufacturability with high-resolution additive manufacturing processes. However, the post-processing applied to stiffness-optimized structures often causes large reduction of stiffness.

2.2. Bi-scale methods

The bi-scale, one-step methods couple micro/meso (*i.e.,* lattice cell) scale and macro (*i.e*., structure) scale optimizations in a nested optimization framework. Coelho et al. [23] combined SIMP and homogenization method to optimize both the micro/meso scale material properties and macro scale density. Chen et al. [24] introduced the moving iso-surface threshold formulation for constructing lattice cells with smooth boundaries, and then optimized a macro-scale structure by homogenization and SIMP. Wang et al. [25] utilized the non-uniform rational B-spline (NURB) basis functions in the finite element analysis to improve the computational accuracy and efficiency of one-step, bi-scale lattice optimization. Wang et al. [26] proposed a parameterized lattice cell to obtain the non-uniform distribution of lattices by iterative calculation with homogenization and SIMP methods. These methods, however, can realize limited spatial variation in lattice cells, which are likely to be sub-optimum. In fact, Panesar et al. [27] showed the structures with graded lattice cells have considerably superior stiffness to the ones with the uniform lattice cells through the experiments with additively-manufactured samples.

To increase the special variation in lattice cells, Radman et al. [28] utilized inverse homogenization for parametrically optimizing three types of lattice cells into functionally graded lattice structures. Daynes et al. [29] optimized the size, aspect ratio and orientation of spatially-varying lattice cells within the SIMP optimized structures based on the isostatic line calculated by the local principal stresses. Li et al. [30] studied the topological design of functionally graded cellular composites with both stiffness and auxetic behaviors by the level set method. For the multi-type cell based optimization, Deng et al. [31] integrated the SIMP at the micro scale and Porous Anisotropic Material with Penalization at the macroscale into a single equation to design bi-scale structures under random field loading. Xu et al. [32] proposed a criterion for the selection of micro heterogeneous materials based on the orientation of the principal stresses. While these methods can realize the lattice cells with high spatial variations, ensuring the connectivity between the optimized lattice cells, especially between the different types, remained as an issue.

In an attempt to overcome this connectivity problem, Wang et al. [33] proposed level-set based shape interpolation of neighboring lattice cells. However, the neighboring cells were constraint to be among a small set of family cells. Nishi et al. [34] proposed bi-scale plate model for topology optimization with multiple types of lattice cells that are designed to connect each other. Campagna et al. [35] separated the design domain into subdomains with solid boundary first, and then filled each domain uniformly with different lattice cells. Du et al. [36] proposed the physics-independent connectivity index between adjacent microstructures and adopted it as a constraint in bi-scale level set topology optimization of microstructure. While these work aimed to achieve high spatial lattice variations with strong cell connectivity, they tend to sacrifice one for another.

The bi-scale, two-step methods first generate a library of various pre-analyzed lattice cells tagged by their homogenized material properties, and then optimizes a structure by "tiling" the lattice cells in the library that match the desired distribution of material properties obtained by topology optimization. Takano et al. [42] constructed a micro–macro correlative database for homogenized properties and employed the genetic algorithm to optimize the graded microstructure. Liang et al. [43] built an approximate constitutive model for local material microstructure using a database model and is further used for multiscale structural topology optimization to reduce the computational cost. Panetta et al. [40] adopted the homogenization method to construct a library connection the microstructure cell with the Poisson's ratio and Young's modulus, and the using a optimization formulation to get the global structure with predefined requirement. Zhu et al. [41] extended the library by level set field method, and added the density variable into the library. Then, they adopted the topology optimization method with the offline library to get global structure. Although two-step optimization can explore a larger number of lattice cells for optimization than one-step optimization, they also suffer from poor connectivity between neighboring cells.

2.3. Buckling-constrained topology optimization

Stability or guard against buckling failure is an important performance metric of structures. It is especially true for lattice structures since they often incorporate slender features that are susceptible to buckling. The structural optimization with buckling constraint was first proposed by Khot et al. [44]. Neves et al. [45] added buckling load constraint into topology optimization to improve both the stiffness and stability of the structure. Luo et al. [46] studied the topology optimization of thin-walled structure with buckling load constraint using a moving iso-surface threshold. Gao et al. [47] studied the SIMP method with buckling constraints for topology optimization. More recently, a new method based on the eigenvalue shift and pseudo mode identification is proposed to reduce the effect of pseudo buckling mode. Dunning et al. [48] proposed the block Jacobi conjugate gradient eigenvalue method to solve the problems of modal shifts for large scale linear buckling analysis, and integrated it into level set based topology optimization framework. Cheng et al. [49] employed buckling constraints for bi-scale topology optimization, where the shape sensitivity of buckling constraints were analyzed in both macro and micro scales. Zhang et al. [50] adopted the moving morphable component (MMC) method to optimize the distribution of stiffening ribs on a given base plate with buckling constraint. Wu et al. [51] proposed the multi-material topology optimization considering both the thermo-mechanical effects and buckling. The results show that the buckling constraints has large influences on the optimized structures. Thomsen et al. [52] employed both the homogenization theory and Floquet–Bloch theory to improve the buckling load of microstructure. Ferrari et al. [53] discussed trade-off between stiffness and buckling requirement in topology optimization and gave recommendations for managing the trade-off.

Despite its importance in lattice structures, previous work in lattice based topology optimization is limited to addressing buckling as post-optimization verification, without explicit incorporation of buckling constraints within optimization.

3. Method

3.1. Density field

The definition of the density field follows the conventional SIMP formulation with Helmholtz regularization [54]. Given a fixed design domain D, characteristic function $X(x)$ of material domain D_Ω is defined as:

$$X(x) = H(\phi(x)) = \begin{cases} 1 & \text{if } x \in D_\Omega \\ 0 & \text{if } x \in D \backslash D_\Omega \end{cases} \tag{1}$$

where x is a point in the design domain D, $\phi: D \to [-1, 1]$ is (un-regularized) density function, and $H: \mathbb{R} \to \{0, 1\}$ is the Heaviside function. To achieve mesh-independency and avoid checkerboard patterns in optimization results, density function ϕ is regularized by the Helmholtz PDE-filter [54,55]:

$$-r^2\nabla^2\overline{\phi} + \overline{\phi} = \phi \tag{2}$$

where r is the filter radius for smoothing, and $\overline{\phi}$ is the smoothed density function. Regularized density field $\rho: D \to \{0, 1\}$ is then defined as:

$$\rho = H(\overline{\phi}) \tag{3}$$

3.2. Averaging radius field

Functionally-graded lattice infill is realized by a continuously variable field of lattice patterns, generated based on the infill optimization method proposed by Wu et al. [20]. In their work, fully-connected lattice patterns are achieved by introducing local volume constraints, which effectively act as setting up many "mini topology optimization" problems within the neighborhood of each design point. In Wu et al. [20], however, local volume is computed as the material density integrated over a circular (or spherical in 3D) domain centered at each design point, with a prescribed *constant* radius. The proposed method, on the other hand, treats this radius as an additional design field, in order to realize spatially-variable field of lattice patterns. Since the numerical integration of local density as

formulated in Wu et al. [20] can be mesh dependent, the proposed method again adopts the Helmholtz PDE-filter to compute locally smoothed, "average" material density field ρ_l:

$$-R^2\nabla^2\rho_l + \rho_l = \rho \tag{4}$$

where R is the filter radius for averaging density around a design point. Together with ϕ in Eq. (2), averaging radius field R is optimized, subject to a constraint on locally averaged density ρ_l:

$$\rho_l \leq P_l \tag{5}$$

where P_l is the prescribed maximum local density. Since the local density constraint in Eq. (5) needs to be defined for every design point, the numerical optimization on the discretized design domain would face difficulty due to a large number of constraints. Alternatively, the constraint can be rewritten as:

$$\max(\rho_l) \leq P_l \tag{6}$$

Since the max operator in Eq. (6) is not differentiable and $0 \leq \rho_l \leq 1$, it is approximated as p-norm function:

$$\left(\int_D \rho_l^p dD\right)^{\frac{1}{p}} \leq P_l \tag{7}$$

As p goes to infinity, Eq. (7) becomes equivalent to Eq. (6), but it will increase the numerical instability of the optimization. In this paper, $p = 10$ is used.

3.3. Buckling constraints

According to the linear bucking theory for a plane continuum structure [56], the linear buckling load factors can be calculated by the following equation:

$$(K + \lambda_j K_\sigma)v_j = 0 \tag{8}$$

where K and K_σ are the global stiffness and geometric matrices, respectively, and λ_j and v_j are the jth buckling load factor and the corresponding buckling mode vector respectively.

The global stiffness matrix K is assembled from element stiffness matrices k_e as:

$$K = \sum_e k_e \tag{9}$$

$$k_e = E_e k_0 \tag{10}$$

$$k_0 = \int B^T B \tag{11}$$

where $\sum$ is the standard finite element assembly operator, E_e is the Young's modulus for each element given by the SIMP power law:

$$E_e = E_{min} + \rho^m(E_0 - E_{min}) \tag{12}$$

and B is the displacement differentiation matrix.

Similarly, the global geometric matrix K_σ is assembled from element geometric matrices k_{ge} as [56]:

$$K_\sigma = \sum_e k_{ge} \tag{13}$$

$$k_{ge} = \int G^T S G \tag{14}$$

where matrices G and S are defined in 2D as:

$$G = \begin{bmatrix} M_1 & M_2 & M_3 & M_4 \end{bmatrix} \tag{15}$$

$$M_i = \begin{bmatrix} \frac{\partial N_i}{\partial x} & \frac{\partial N_i}{\partial y} & 0 & 0 \\ 0 & 0 & \frac{\partial N_i}{\partial x} & \frac{\partial N_i}{\partial y} \end{bmatrix}^T \quad \text{for } i = 1, 2, 3, 4 \tag{16}$$

$$S = \begin{bmatrix} \sigma_x & \tau_{xy} & 0 & 0 \\ \tau_{xy} & \sigma_y & 0 & 0 \\ 0 & 0 & \sigma_x & \tau_{xy} \\ 0 & 0 & \tau_{xy} & \sigma_y \end{bmatrix} \tag{17}$$

where $N_i\ (x, y)$ is element shape functions. To overcome the problem of local modes in void area for linear buckling analysis, stresses in matrix S in Eq. (15) is calculated by the Young's modulus E_e in Eq. (11) multiplied by the nth power of element density ρ:

$$\sigma = E_{ge} B u \tag{18}$$

$$E_{ge} = \rho^n E_e \tag{19}$$

where u is the displacement vector. If m and n are set as the same value, they will cause instability during optimization. Hence, in this paper, $m = 3$ and $n = 5$ are used.

While the buckling load factors computed by Eq. (8) may have both positive and negative values, their magnitude represents the level of safety margins against buckling failures. Therefore only $\lambda_j > 0$ is considered for identifying the most critical bucking mode with the minimum load factor. Hence the bucking constraint is written as:

$$\min_{j \in i | \overline{\lambda}_i > 0} \overline{\lambda_j} \geq \lambda^* \tag{20}$$

$$\overline{\lambda_j} = \frac{\lambda_j}{\lambda_c} \tag{21}$$

where λ^* is a prescribed minimum safety margin and λ_c is the minimum positive buckling load factor of the equivalent structure obtained by the SIMP method.

3.4. Optimization model

Based on the definitions of design fields and constraints, an optimization model for functionally graded lattice structure is formulated as follows:

$$\begin{aligned} \underset{(\phi, R)}{\text{minimize}} \quad & F(u) \\ \text{subject to:} \quad & Ku = f \\ & -r^2 \nabla^2 \overline{\phi} + \overline{\phi} = \phi \\ & -R^2 \nabla^2 \rho_l + \rho_l = \rho \\ & \int_D \rho \, dD \leq V \\ & \left(\int_D \rho_l^p \, dD \right)^{\frac{1}{p}} \leq P_l \\ & \min_{j \in i | \overline{\lambda}_i > 0} \overline{\lambda_j} \geq \lambda^* \\ & -1 \leq \phi \leq 1 \\ & R_{min} \leq R \leq R_{max} \end{aligned} \tag{22}$$

where $F(u)$ is the objective function, f is external force, V is the prescribed maximum total volume, R_{min} and R_{max} are the lower and upper bounds for R, respectively. Naturally, R_{min} should be set larger than r. In case of the minimization of the structure compliance, the object function can be written as:

$$F(u) = f^T u = \frac{1}{2} u^T K u \tag{23}$$

3.5. Sensitivities

3.5.1. Sensitivities of the Helmholtz PDE-filter

For Eqs. (2) and (4), we follow the same sensitivities derivation method of Lazarov and Sigmund [54]. For example, the finite element discretization of the Helmholtz PDE-filter function in Eq. (2) yields a linear equation

for unknown values of the filtered field:

$$K_f \overline{\phi} = P_\phi \tag{24}$$

$$K_f = \sum_e k_{fe} \tag{25}$$

$$P_\phi = \sum_e P_{\phi e} \tag{26}$$

where $\sum$ is the standard finite element assembly operator and

$$k_{fe} = \int \left(-\nabla N^T r^2 \nabla N + N^T N\right) d\Omega_e \tag{27}$$

$$P_{\phi e} = \int N \phi d\Omega_e \tag{28}$$

The finite element discretization of Eq. (4) is derived in a similar manner. Then, the sensitivities of filtered density $\overline{\phi}$ with respect to design variables ϕ and R are given respectively as:

$$\frac{\partial \overline{\phi}}{\partial \phi} = \left\{\sum \int \left(-\nabla N^T r^2 \nabla N + N^T N\right) d\Omega_e\right\}^{-1} \cdot \left\{\sum \int N d\Omega_e\right\} \tag{29}$$

$$\frac{\partial \overline{\phi}}{\partial R} = 0 \tag{30}$$

Using the chain rule, the sensitivity of locally-averaged density ρ_l with respect to ϕ can be obtained as:

$$\frac{\partial \rho_l}{\partial \phi} = \frac{\partial \rho_l}{\partial \rho} \frac{\partial \rho}{\partial \overline{\phi}} \frac{\partial \overline{\phi}}{\partial \phi} \tag{31}$$

$$\frac{\partial \rho_l}{\partial \rho} = \left\{\sum \int \left(-\nabla N^T R^2 \nabla N + N^T N\right) d\Omega_e\right\}^{-1} \cdot \left\{\sum \int N d\Omega_e\right\} \tag{32}$$

$$\frac{\partial \rho}{\partial \overline{\phi}} = \frac{\partial H(\overline{\phi})}{\partial \overline{\phi}} = \delta(\overline{\phi}) \tag{33}$$

Substituting Eqs. (31), (32), and (28) into Eq. (30) yields:

$$\begin{aligned}\frac{\partial \rho_l}{\partial \phi} = &\left\{\sum \int \left(-\nabla N^T R^2 \nabla N + N^T N\right) d\Omega_e\right\}^{-1} \cdot \left\{\sum \int N d\Omega_e\right\} \cdot \delta\left(\overline{\phi}\right) \\ &\cdot \left\{\sum \int \left(-\nabla N^T r^2 \nabla N + N^T N\right) d\Omega_e\right\}^{-1} \cdot \left\{\sum \int N d\Omega_e\right\}\end{aligned} \tag{34}$$

Finally, the sensitivity of ρ_l with respect to R is given as:

$$\frac{\partial \rho_l}{\partial R} = \left\{\sum \int \left(-\nabla N^T R^2 \nabla N + N^T N\right) d\Omega_e\right\}^{-1} \cdot \left\{\sum \int 2R \nabla N^T \nabla N d\Omega_e\right\} \cdot \rho_l \tag{35}$$

3.5.2. Sensitivities of the objective function and the constraints

In this paper, the compliance of the structure is used as the objective function, for which the sensitivities with respect to design variables ϕ and R can be calculated using the adjoint method:

$$\begin{aligned}\frac{\partial F(u)}{\partial \phi} &= \frac{\partial F(u)}{\partial \rho} \frac{\partial \rho}{\partial \overline{\phi}} \frac{\partial \overline{\phi}}{\partial \phi} \\ &= -m \cdot u^T \rho^{m-1} u \cdot \delta\left(\overline{\phi}\right) \cdot \left\{\sum \int \left(-\nabla N^T r^2 \nabla N + N^T N\right) d\Omega_e\right\}^{-1} \cdot \left\{\sum \int N d\Omega_e\right\}\end{aligned} \tag{36}$$

$$\frac{\partial F(u)}{\partial R} = \frac{\partial F(u)}{\partial \rho} \frac{\partial \rho}{\partial \overline{\phi}} \frac{\partial \overline{\phi}}{\partial R} = 0 \tag{37}$$

The sensitivities of the constraints on the total material volume in Eq. (21) with respect to design variables ϕ and R are given respectively as:

$$\frac{\partial V}{\partial \phi} = \frac{\partial V}{\partial \rho}\frac{\partial \rho}{\partial \overline{\phi}}\frac{\partial \overline{\phi}}{\partial \phi} = \delta(\overline{\phi}) \cdot \left\{\sum \int \left(-\nabla N^T r^2 \nabla N + N^T N\right) d\Omega_e\right\}^{-1} \cdot \left\{\sum \int N d\Omega_e\right\} \tag{38}$$

$$\frac{\partial V}{\partial R} = \frac{\partial V}{\partial \rho}\frac{\partial \rho}{\partial \overline{\phi}}\frac{\partial \overline{\phi}}{\partial R} = 0 \tag{39}$$

The sensitivities of the constraints on the local density in Eq. (21) with respect to design variables ϕ and R are given respectively as:

$$\frac{\partial P_l}{\partial \phi} = \frac{\partial P_l}{\partial \rho_l}\frac{\partial \rho_l}{\partial \rho}\frac{\partial \rho}{\partial \overline{\phi}}\frac{\partial \overline{\phi}}{\partial \phi} \tag{40}$$

$$\frac{\partial P_l}{\partial R} = \frac{\partial P_l}{\partial \rho_l}\frac{\partial \rho_l}{\partial R} \tag{41}$$

where

$$\frac{\partial P_l}{\partial \rho_l} = \rho_l^{m-1}\left(\sum \rho_l^m\right)^{\frac{1}{m-1}} \tag{42}$$

Substituting Eqs. (41), (31), (32), and (28) into Eq. (39) gives:

$$\begin{aligned}\frac{\partial P_l}{\partial \phi} = {} & \rho_l^{m-1}\left(\sum \rho_l^m\right)^{\frac{1}{m-1}} \cdot \left\{\sum \int \left(-\nabla N^T R^2 \nabla N + N^T N\right) d\Omega_e\right\}^{-1} \cdot \left\{\sum \int N d\Omega_e\right\} \cdot \delta\left(\overline{\phi}\right) \\ & \cdot \left\{\sum \int \left(-\nabla N^T r^2 \nabla N + N^T N\right) d\Omega_e\right\}^{-1} \cdot \left\{\sum \int N d\Omega_e\right\}\end{aligned} \tag{43}$$

Substituting Eqs. (34) and (41) into Eq. (40) gives:

$$\begin{aligned}\frac{\partial V_l}{\partial R} = {} & \rho_l^{m-1}\left(\sum \rho_l^m\right)^{\frac{1}{m-1}} \cdot \left\{\sum \int \left(-\nabla N^T R^2 \nabla N + N^T N\right) d\Omega_e\right\}^{-1} \\ & \cdot \left\{\sum \int 2R \nabla N^T \nabla N d\Omega_e\right\} \cdot \rho_l\end{aligned} \tag{44}$$

3.5.3. Sensitivities of buckling load factors

The sensitivity of the buckling load is not straightforward to compute. While most papers used the partial derivative of the geometric matrix with respect to the density field as part of the sensitivities [47,53], it is still quite complicated to compute the sensitivity of the stress vector with respect to the density field. We therefore followed the derivation in [57], where adjoint variables are added to constraint equations:

$$v_j^T(K + \lambda_j K_\sigma)v_j + \mu^T\left(\sigma - \rho^n E_e B u\right) + \omega^T(B^T E_e B u - f) = 0 \tag{45}$$

where μ and ω are the adjoint variables. Differentiating Eq. (43) with respect to the density field yields:

$$\begin{aligned}& 2\left(\frac{\partial v_j}{\partial \rho}\right)^T (K + \lambda_j K_\sigma)v_j + v_j^T\left(\frac{\partial K}{\partial \rho} + \frac{\partial \lambda_j}{\partial \rho}K_\sigma + \lambda_j \frac{\partial K_\sigma}{\partial \sigma}\frac{\partial \sigma}{\partial \rho}\right)v_j \\ & \quad + \mu^T\left(\frac{\partial \sigma}{\partial \rho} - \frac{\partial E_{ge}}{\partial \rho}Bu - E_{ge}B\frac{\partial u}{\partial \rho}\right) + \omega^T\left(B^T\frac{\partial E_e}{\partial \rho}Bu + B^T E_e B\frac{\partial u}{\partial \rho}\right) = 0\end{aligned} \tag{46}$$

and rearranging:

$$\begin{aligned}& \left(\lambda_j v_j^T\frac{\partial K_\sigma}{\partial \sigma}v_j + \mu^T\right)\frac{\partial \sigma}{\partial \rho} + v_j^T\frac{\partial K}{\partial \rho}v_j + v_j^T\frac{\partial \lambda_j}{\partial \rho}K_\sigma v_j - \mu^T\left(\frac{\partial E_{ge}}{\partial \rho}Bu + E_{ge}B\frac{\partial u}{\partial \rho}\right) \\ & \quad + \omega^T\left(B^T\frac{\partial E_e}{\partial \rho}Bu + B^T E_e B\frac{\partial u}{\partial \rho}\right) = 0\end{aligned} \tag{47}$$

By choosing adjoint variable μ so that the coefficient of $\frac{\partial \sigma}{\partial \rho}$ is equal to zero, we get:

$$\mu^T = -\lambda_j v_j^T\frac{\partial K_\sigma}{\partial \sigma}v_j \tag{48}$$

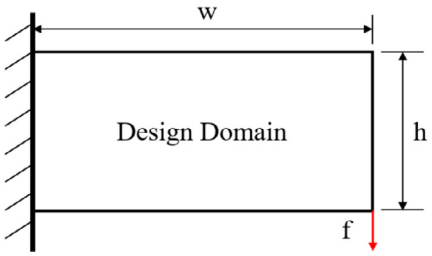

Fig. 1. Design domain and boundary condition for the cantilever beam example.

Substituting Eq. (47) to Eq. (46) and similarly choosing adjoint variable ω so that the coefficient of $\frac{\partial u}{\partial \rho}$ is equal to zero, we get:

$$\omega^T = (\mu^T E_{ge} B)(B^T E_e B)^{-1} \tag{49}$$

The sensitivity for buckling load factor λ_j with respect to the density field is then obtained by Eqs. (45), (47) and (48):

$$\frac{\partial \lambda_j}{\partial \rho} = -\frac{v_j^T \frac{\partial K}{\partial \rho} v_j - \mu^T \frac{\partial E_{ge}}{\partial \rho} Bu + \omega^T B^T \frac{\partial E_e}{\partial \rho} Bu}{v_j^T K_\sigma v_j} \tag{50}$$

Finally, combining Eqs. (29), (30), (33), and (49), the sensitivity for buckling with respect to design variables ϕ and R can be obtained as:

$$\frac{\partial \lambda_j}{\partial \phi} = \frac{\partial \lambda_j}{\partial \rho}\frac{\partial \rho}{\partial \overline{\phi}}\frac{\partial \overline{\phi}}{\partial \phi} = -\frac{v_j^T \frac{\partial K}{\partial \rho} v_j - \mu^T \frac{\partial \overline{E}}{\partial \rho} Bd + \omega^T B^T \frac{\partial E}{\partial \rho} Bd}{v_j^T K_\sigma v_j} \cdot \delta\left(\overline{\phi}\right) \cdot \left[\sum \int \left(-\nabla N^T r^2 \nabla N + N^T N\right) d\Omega_e\right]^{-1} \cdot \left[\sum \int N d\Omega_e\right] \tag{51}$$

$$\frac{\partial \lambda_j}{\partial R} = \frac{\partial \lambda_j}{\partial \rho}\frac{\partial \rho}{\partial \overline{\phi}}\frac{\partial \overline{\phi}}{\partial R} = 0 \tag{52}$$

In case there are multiple minimum eigenvalues occurred during optimization, the strategies proposed by Gravesen et al. [58] is adopted. If the computation resource is sufficient, buckling constraints based on the aggregation functions by Ferrari et al. [53] can also be used.

4. Examples

This section presents numerical examples for demonstrating the proposed method. Section 4.1 discusses examples on a cantilever beam and a MBB beam, for examining the effect of variable radius R for local density averaging without buckling constraints on the optimized structures. Section 4.2 discusses examples on the same cantilever and a column-like structure under distributed loads, for examining the effect of buckling constraints on the optimized structures. In all examples, MATLAB and COMSOL Multiphysics are used to model the problem, and the MMA optimization solver [59] is adopted to solve the optimization problem.

4.1. Functionally-graded lattice structures without buckling constraints

The first example is a cantilever beam. The design domain in Fig. 1 is defined as a rectangle area of unit thickness with width $w = 2$ and height $h = 1$ fixed at the left side. A concentrated load $f = 1$ is applied at the lower right vertex of the rectangle. The design domain is discretized into 200×100 equally-sized square four-node element with Young's modulus $E = 1$ and Poisson's ratio $\nu = 0.3$. The filter radius r is set as the element size, and $V = 0.5$ and $P_l = 0.6$ are used.

Fig. 2 shows the snapshots for the convergence history of functionally-graded lattice patterns at different iterations during optimization. The density field is initialized uniformly with 0.5 over the entire design domain. The bounds

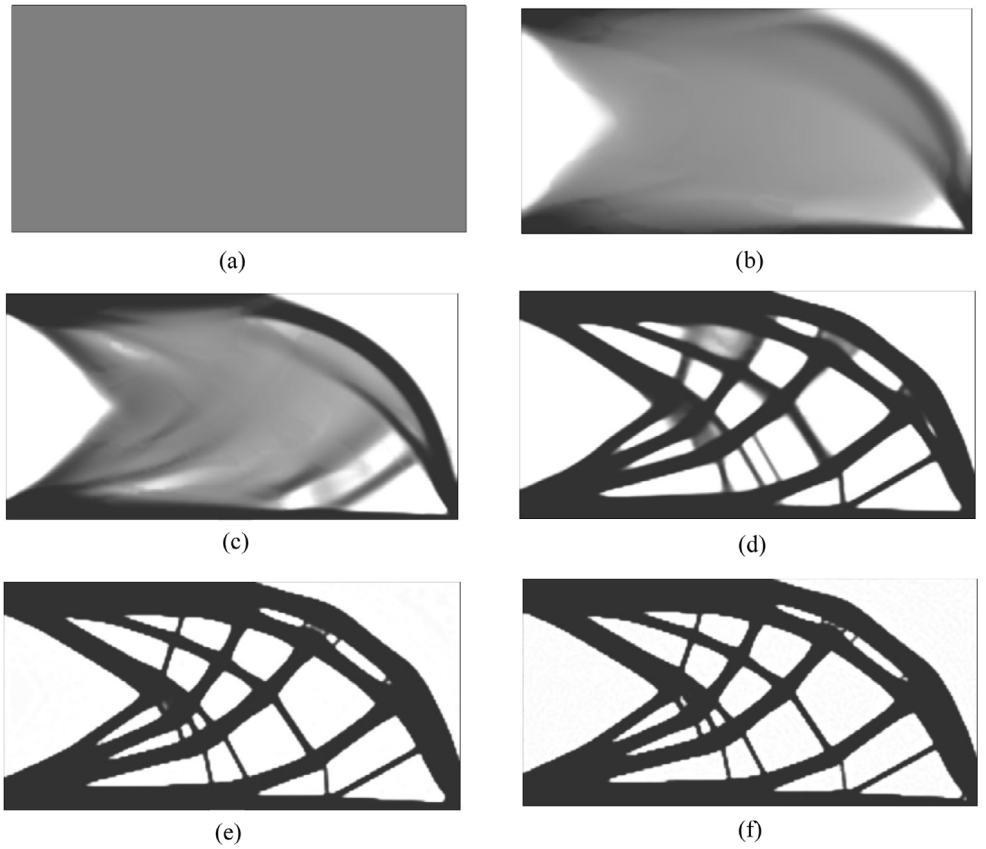

Fig. 2. Iteration details for $r \leq R \leq 20r$ without buckling constraints. (a) initialization, (b) iteration 10, (c) iteration 20, (d) iteration 40, (e) iteration 80, and (f) iteration 150.

for averaging radius R are set as $R_{min} = r$ and $R_{max} = 20r$. The result at iteration 200 is shown in Fig. 3(b), and the result for SIMP with the same initialization, at the same number of iterations, maximum total volume, and filter radius are shown in Fig. 3(a). Local density ρ_l and averaging radius R after optimization are shown in Figs. 3(c) and 3(d), respectively. It can be seen in Fig. 3(c) that most of the local density is smaller than $P_l = 0.6$. Compared to the SIMP result, the proposed method can produce solid near the periphery of the structure where stiffness is needed, and functionally-graded lattice in the middle of the structure where stability against buckling is desired (although buckling constraints are not included in this example). The compliance of the result in Fig. 3(b) is 0.1858 (it is a normalized compliance, which is the compliance of current iterations divided by that of the first iteration), only slightly worse than 0.1847 for the SIMP result in Fig. 3(a).

The convergence history of the optimization process is plotted in Fig. 4. The normalized compliance (red line) starts at 1.0, decreases rapidly to approximately 0.2 within 40 iterations. It converges approximately at 80 iterations and remains stable afterwards. The total volume (green line) starts at 0.5 as initialized and stays there after a few iterations of oscillation. The local density (black line) starts at 0.5 and converge rapidly to 0.6 within 20 iterations.

To examine the benefit of functionally-graded lattice over the constant lattice, the optimization results with variable and constant averaging radius are compared. Table 2 shows the normalized compliance values of the tested results with various values (for constant lattice) and ranges (for functionally-graded lattice) of averaging radius R, and Fig. 5 shows the corresponding optimal structures for each case in Table 2. The normalized compliance values of the functionally-graded lattice structures are better than the constant lattice for each comparison case. It is expected since the optimization problem with variable R (functionally-graded lattice) is a relaxation of the optimization problem with constant R (constant lattice). It is also observed that the normalized compliance values improve as the value (for constant lattice) and range (for functionally-graded lattice) of R becomes larger. In particular, the

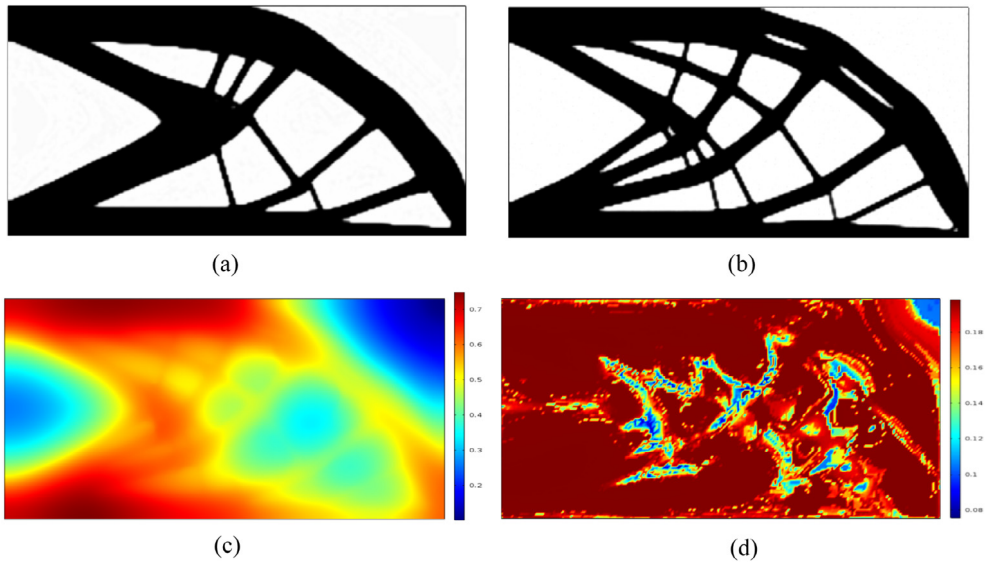

Fig. 3. Comparison of SIMP and the proposed method with $r \leq R \leq 20r$ without buckling constraints after 200 iterations; (a) SIMP, (b) functionally-graded lattice, (c) local density ρ_l, and (d) averaging radius R.

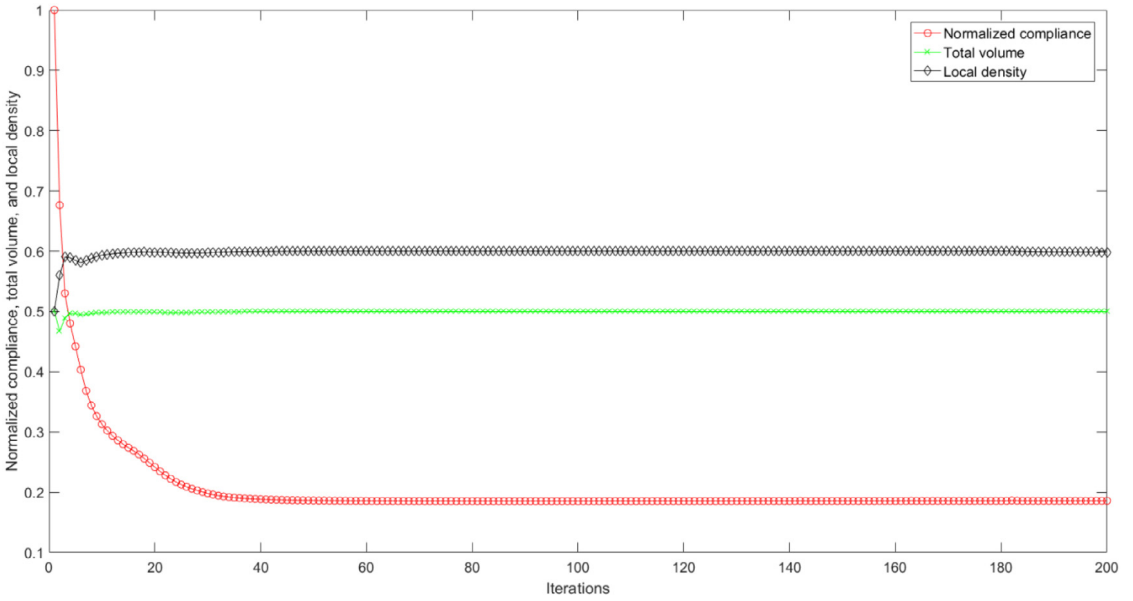

Fig. 4. Convergence history for $r \leq R \leq 20r$, without buckling constraints . (For interpretation of the references to color in this figure legend, the reader is referred to the web version of this article.)

normalized compliance values for the case with $r \leq R \leq 60r$ is almost the same as the one for SIMP (0.1847), although the resulting structures look quite different.

The second example is the MBB beam. The design domain in Fig. 6 is defined as a rectangle area of unit thickness with width $w = 3$ and height $h = 1$, simply-supported at the bottom corners. A concentrated load $f = 1$ is applied at the middle of the upper side of the rectangle. The design domain is discretized into 300×100 equally-sized square four-node element with Young's modulus $E = 1$ and Poisson's ratio $\nu = 0.3$. The filter radius r is set as the element size, and $V = 0.5$ and $P_l = 0.6$ are used.

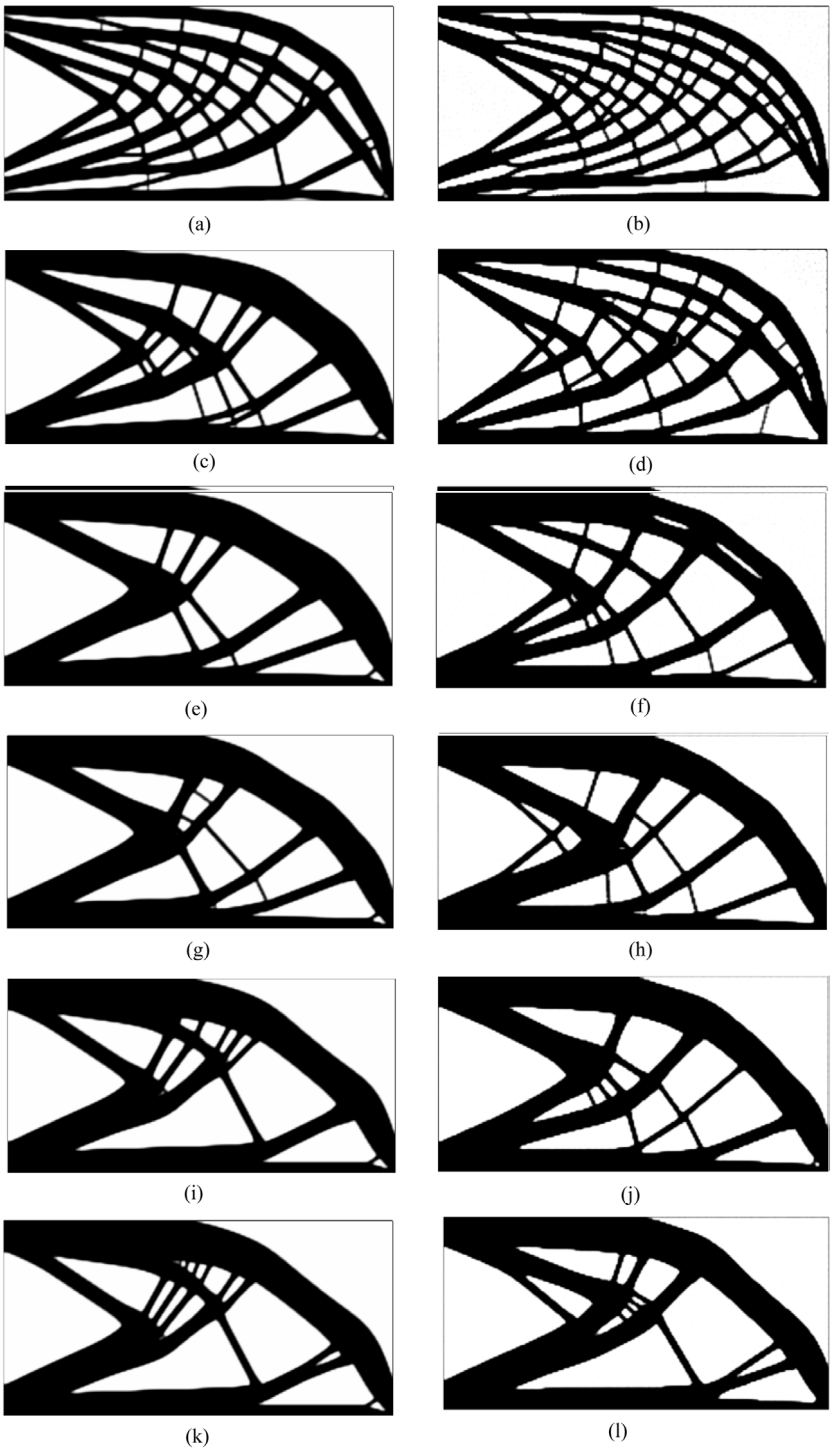

Fig. 5. Comparisons of constant lattice and functionally-graded lattice cantilever beams without buckling constraints; (a) $R = 5r$, (b) $r \leq R \leq 5r$, (c) $R = 10r$, (d) $r \leq R \leq 10r$, (e) $R = 20r$, (f) $r \leq R \leq 20r$, (g) $R = 30r$, (h) $r \leq R \leq 30r$, (i) $R = 40r$, (j) $r \leq R \leq 40r$, (k) $R = 60r$, and (l) $r \leq R \leq 60r$.

Table 2
Comparisons of constant lattice and functionally-graded lattice cantilever beams without buckling constraints.

Constant lattice	Compliance	Functionally-graded lattice	Compliance
$R = 5r$	0.2299	$r \leq R \leq 5r$	0.2097
$R = 10r$	0.2167	$r \leq R \leq 10r$	0.2045
$R = 20r$	0.2015	$r \leq R \leq 20r$	0.1858
$R = 30r$	0.1902	$r \leq R \leq 30r$	0.1857
$R = 40r$	0.1901	$r \leq R \leq 40r$	0.1856
$R = 60r$	0.1895	$r \leq R \leq 60r$	0.1853

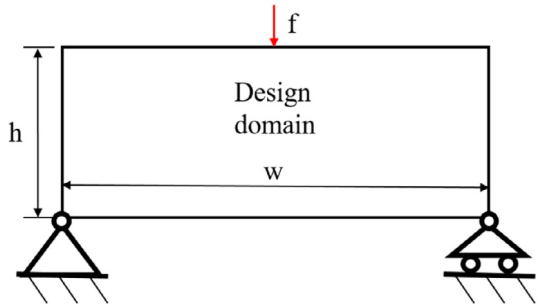

Fig. 6. Design domain and boundary condition for MBB problem.

Fig. 7 shows the optimized structures with various values (for constant lattice) and ranges (for functionally-graded lattice) of averaging radius R. The normalized compliance values of the functionally-graded lattice structures are again better than the constant lattice structures, with more significant improvement than the cantilever example. Similarly, it is also observed that the normalized compliance values improve as the value (for constant lattice) and range (for functionally-graded lattice) of R becomes larger. It should be noted that in this particular example, all functionally-graded lattice structures in Fig. 7, except for the one with $r \leq R \leq 5r$, achieved smaller normalized compliance values than the one for SIMP. While mathematically it should not be the case (since the SIMP is a relaxation of the optimization problem with variable R), an additional constraint on the average local density could have helped rearranging the material appropriately during optimization to improve the compliance at the convergence.

4.2. Functionally-graded lattice structures with buckling constraints

Firstly, the cantilever beam example in Section 4.1. is further examined in terms of the stability against buckling. Fig. 8 shows the buckling modes (scaling factor = 0.005) and the minimum (normalized) buckling load factor $\bar{\lambda}$ defined in Eq. (2) for each of the structures in Fig. 5 (except for R = 60r, which is practically identical to SIMP) and SIMP in Fig. 3. As a baseline for comparison, Fig. 8(k) shows the buckling mode for SIMP, which has the minimum (normalized) buckling load factor equals to 1. The local buckling is observed at the long thin bar at the bottom right which is under compression. It can be seen that, for both constant lattices and functionally-graded lattices, averaging radius R larger than $10r$ shows almost no influence on the structural stability. In particular, the structural stability of functionally-graded lattices is consistently lower than that of constant lattices and SIMP. This suggests the functionally-graded lattices require the explicit inclusion of the buckling constraints in order to take full advantage of the relaxed design space, which is attempted below.

Secondly, the cantilever example with $r \leq R \leq 30r$ is solved with the buckling constraints with $\lambda^* = 2.60$, in order to examine the improvement of the structural stability over the cases without them. The adaptive threshold for Heaviside function are used and set as 0.75, 0.6, 0.45, and 0.3 for iterations of 1–50, 50–150, 150–300, and 300–600 iterations, respectively. Fig. 9 shows the snapshots of the evolution of the structure during optimization. Compared to the snapshots of optimization in Fig. 2 for the same example without the buckling constraints, this case required far more iterations for convergence. It can also be seen that the structure evolves first by solidifying

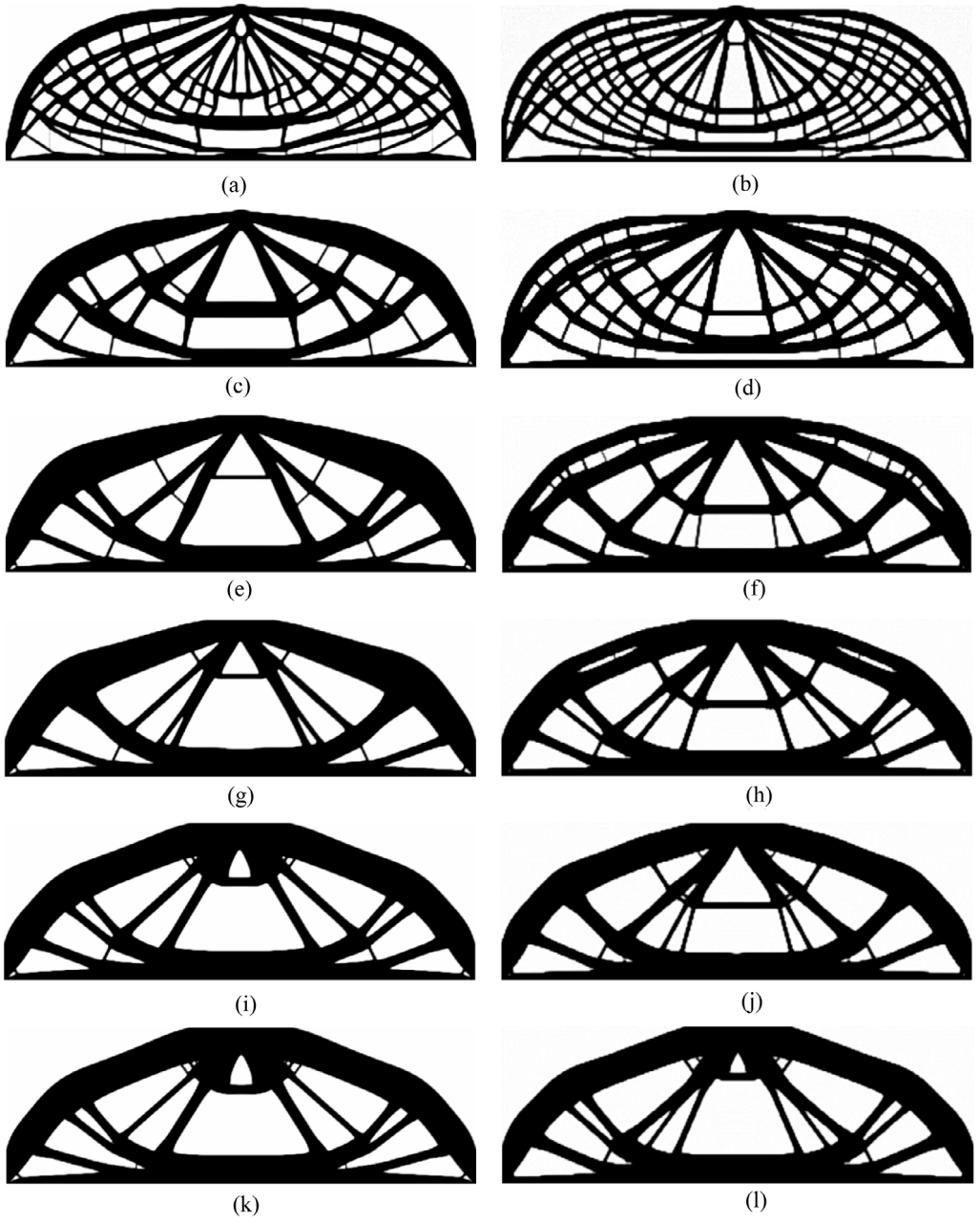

Fig. 7. Comparisons of constant lattice and functionally-graded lattice MBB beams without buckling constraints; (a) $R = 5r$ (c = 0.2254), (b) $r \leq R \leq 5r$ (c = 0.2054), (c) $R = 10r$ (c = 0.2115), (d) $r \leq R \leq 10r$ (c = 0.1903), (e) $R = 20r$ (c = 0.1961), (f) $r \leq R \leq 20r$ (c = 0.1812), (g) $R = 30r$ (c = 0.1922), (h) $r \leq R \leq 30r$ (c = 0.1798), (i) $R = 40r$ (c = 0.1908), (j) $r \leq R \leq 40r$ (c = 0.1797), (k) SIMP (c = 0.1913), and (l) $r \leq R \leq 60r$ (c = 0.1791).

its periphery while leaving grays inside, and then by turning the grays to a functionally-graded lattice pattern. The optimized result at the convergence exhibits long thick members transversely supported by short thin members along their length, which would contribute to higher structural stability without sacrificing stiffness.

The convergence history of the optimization process is plotted in Fig. 10. The normalized compliance (red line) decreases rapidly within 100 iterations while the solid material is being formed at the periphery. Then, it keeps decreasing slowly until approximately 500 iterations. The normalized compliance of the optimized structure is

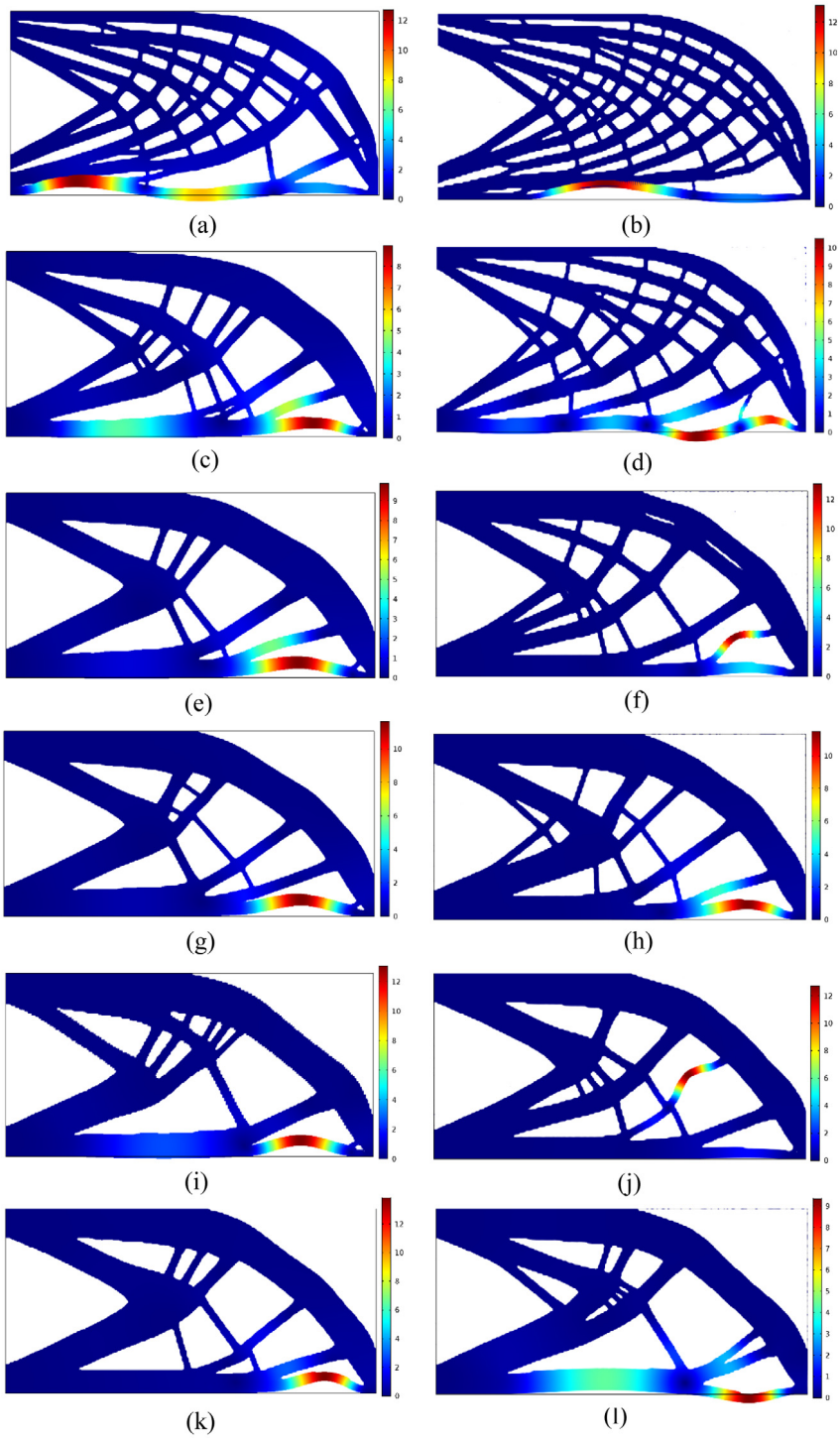

Fig. 8. Comparison of buckling mode of some structures in Fig. 5 and SIMP; (a) $R = 5r$, $\overline{\lambda} = 0.3902$, (b) $r \leq R \leq 5r$, $\overline{\lambda} = 0.1336$, (c) $R = 10r$, $\overline{\lambda} = 1.1432$, (d) $r \leq R \leq 10r$, $\overline{\lambda} = 0.8299$, (e) $R = 20r$, $\overline{\lambda} = 1.1080$, (f) $r \leq R \leq 20r$, $\overline{\lambda} = 0.8097$, (g) $R = 30r$, $\overline{\lambda} = 1.0423$, (h) $r \leq R \leq 30r$, $\overline{\lambda} = 0.7724$, (i) $R = 40r$, $\overline{\lambda} = 1.0174$, (j) $r \leq R \leq 40r$, $\overline{\lambda} = 0.8699$, (k) SIMP, $\overline{\lambda} = 1$, and (l) $r \leq R \leq 60r$, $\overline{\lambda} = 0.8195$.

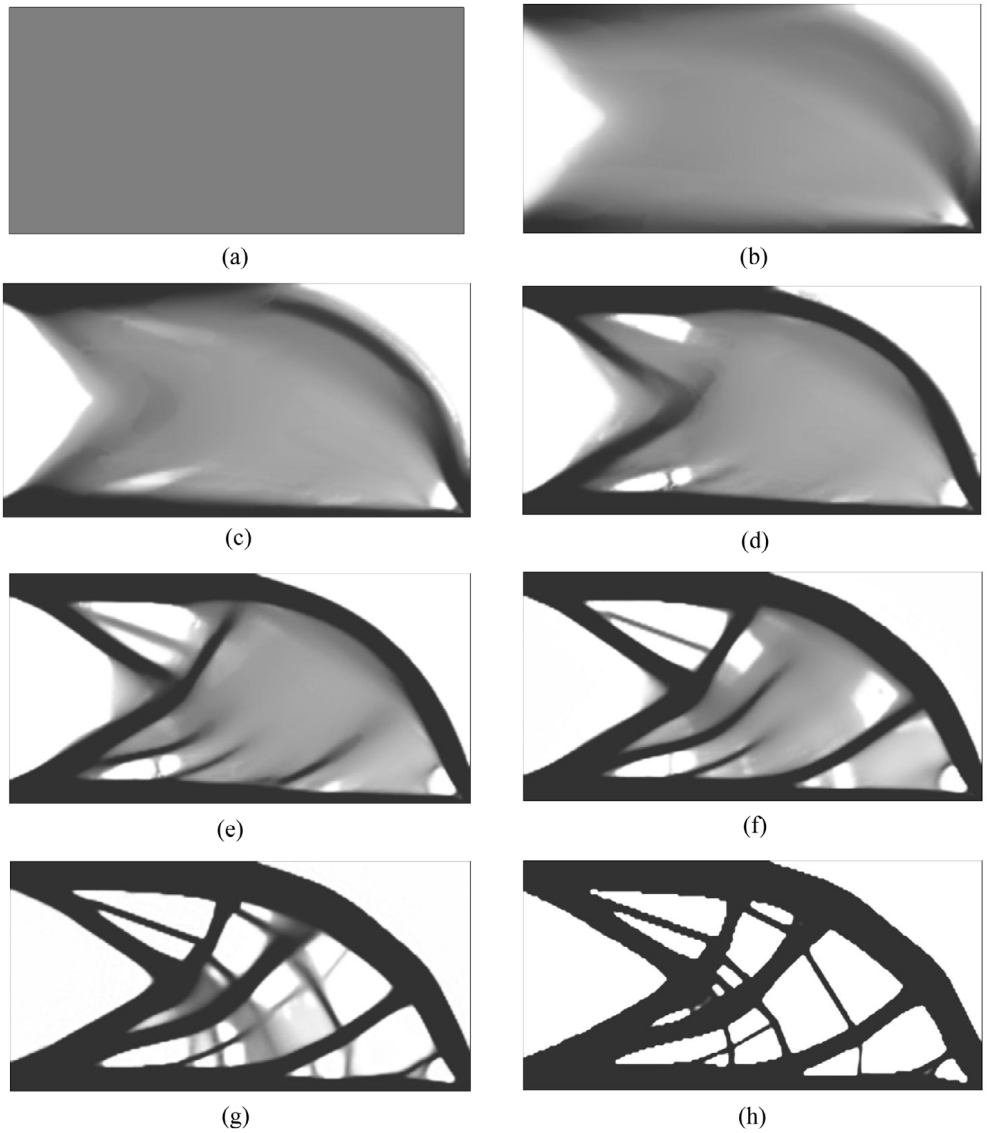

Fig. 9. Iteration details for $r \leq R \leq 30r$ with buckling constraints ($\lambda^* = 2.60$); (a) initialization, (b) iteration 10, (c) iteration 20, (d) iteration 40, (e) iteration 80, (f) iteration 150, (g) iteration 300, and (h) iteration 600.

0.1872, which is very close to the one without buckling constraint, 0.1857 in Table 2. The slow convergence is due to the exploration of the lattice patterns that balance stiffness and stability, as observed in the oscillations of buckling constraint (blue line) which eventually converges to 2.6 at around 500 iterations. The total volume (green line) starts at 0.5 as initialized and stays there with almost no oscillation. The local density (black line) starts at 0.5 and converge rapidly to 0.6 within 20 iterations.

Figs. 11–14 show the optimized structures with $r \leq R \leq 20r$ and different levels of stability margins, $\lambda^* = 1.8, 2.6, 3.7, 5.0$, respectively. In subfigures (b), the scaling factor is set as 0.005. In subfigures (c), tensile stresses are shown in red and compressive stress are shown in blue, with the scale ratio for the magnitude of the tension and compression being 0.004. The buckling constraints are satisfied for the cases with $\lambda^* = 1.8, 2.6, 3.7$ (Figs. 11–13) and slightly violated (4.57) for the case with $\lambda^* = 5.0$ (Fig. 14).

It can be seen in subfigures (a) that the optimized structures exhibit more lattices as the safety margin λ^*increases, while consistently achieving the comparable compliance to the cases without buckling constraints in Fig. 5, and

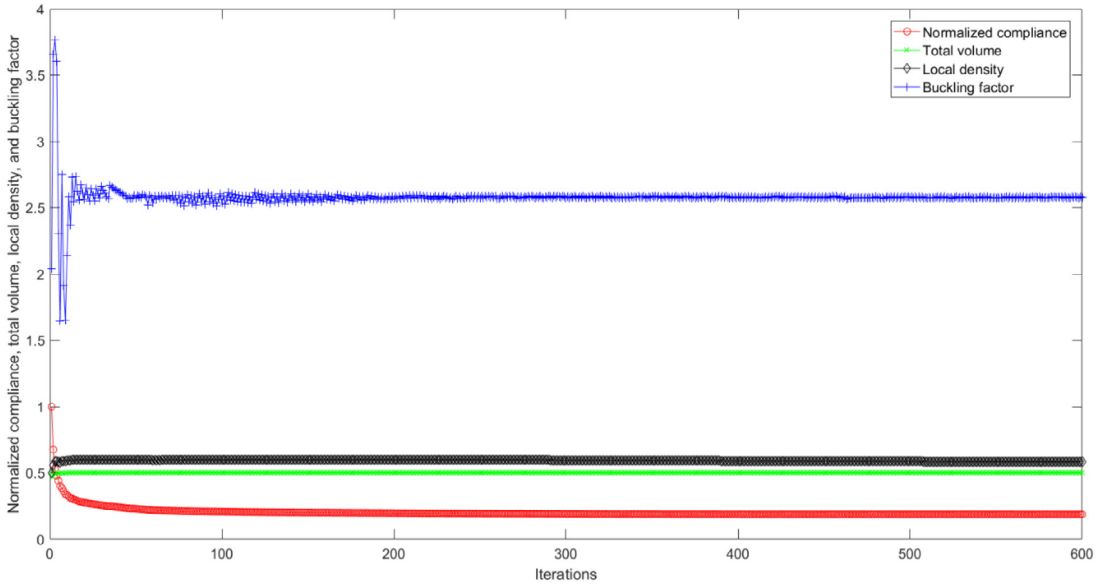

Fig. 10. Convergence history for $r \leq R \leq 30r$ with buckling constraints ($\lambda^* = 2.60$) . (For interpretation of the references to color in this figure legend, the reader is referred to the web version of this article.)

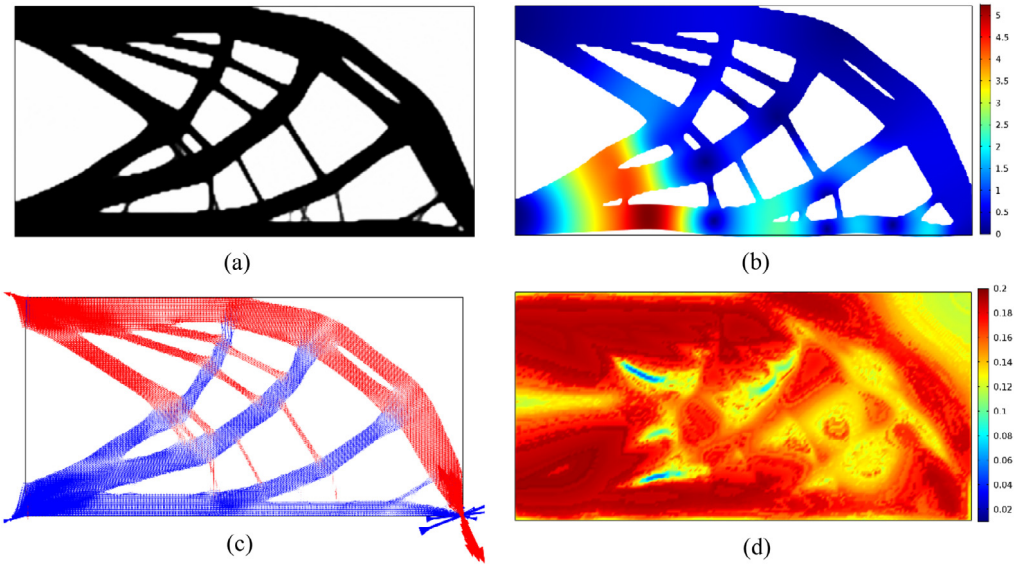

Fig. 11. Functionally-graded lattice cantilever beams with $r \leq R \leq 20r$ and $\lambda^* = 1.8$: (a) Optimized structure (compliance = 0.1858), (b) buckling mode, (c) principal stress, and (d) averaging radius R . (For interpretation of the references to color in this figure legend, the reader is referred to the web version of this article.)

very close to SIMP. The principal stresses in subfigures (b) confirm the observation for the result in Fig. 9: the long thick members under compression (blue) are transversely supported by short thin members along their length, which are primarily under tension. As the level of stability margin increases, a larger number of short thin members (i.e., more lattices) are added, in order to further reduce the risk of local buckling. Subfigures (d) indeed indicate the optimized structures utilize smaller averaging radius that would create more lattices, as the level of stability margin increases.

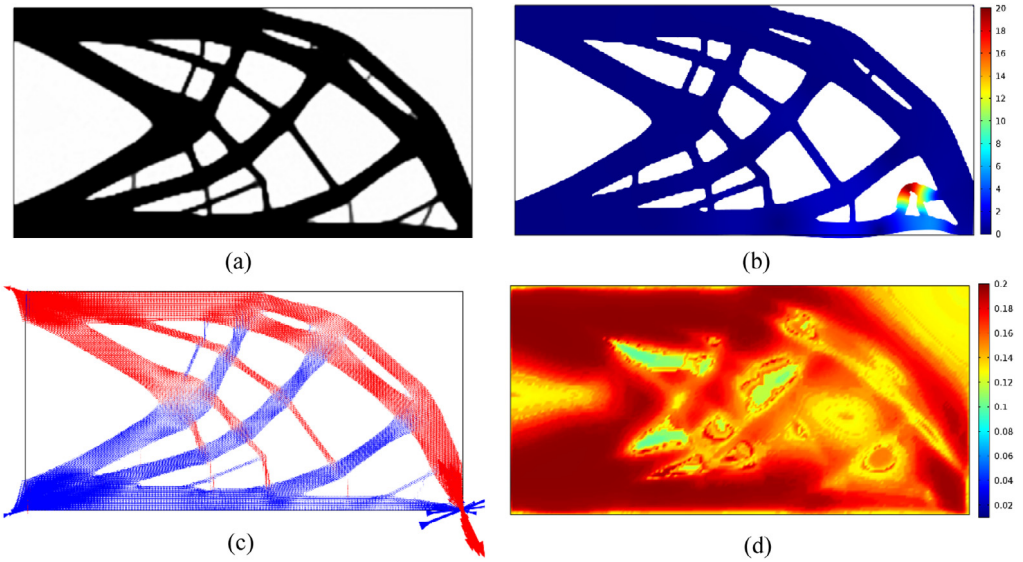

Fig. 12. Functionally-graded lattice cantilever beams with $r \leq R \leq 20r$ and $\lambda^* = 2.6$: (a) Optimized structure (compliance = 0.1874), (b) buckling mode, (c) principal stress, and (d) averaging radius R . (For interpretation of the references to color in this figure legend, the reader is referred to the web version of this article.)

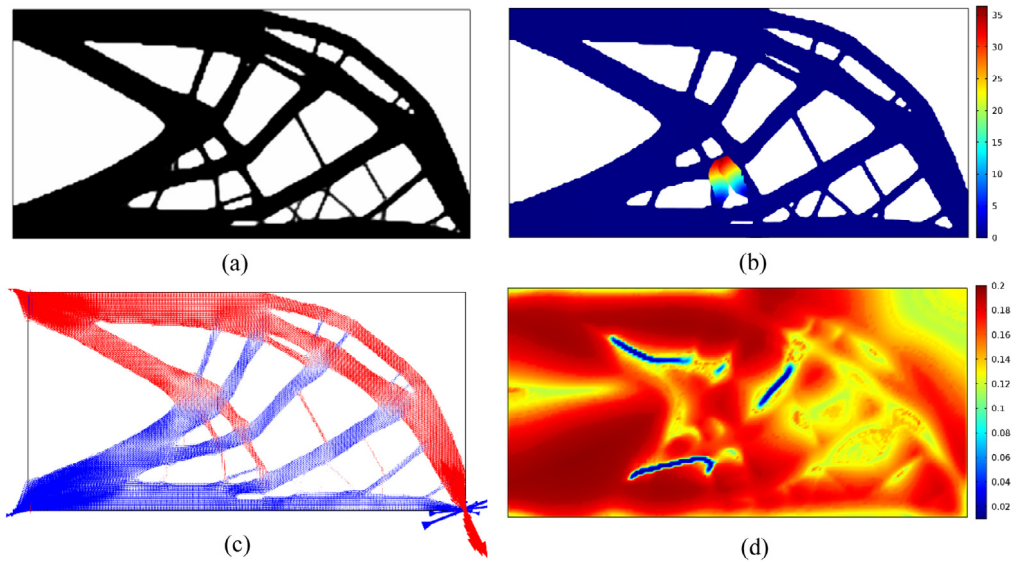

Fig. 13. Functionally-graded lattice cantilever beams with $r \leq R \leq 20r$ and $\lambda^* = 3.7$: (a) Optimized structure (compliance = 0.1875), (b) buckling mode, (c) principal stress, and (d) averaging radius R . (For interpretation of the references to color in this figure legend, the reader is referred to the web version of this article.)

Figs. 15–18 show the optimized structures with $r \leq R \leq 30r$ and different levels of stability margins, $\lambda^* = 1.8, 2.6, 3.7, 5.0$, respectively. The overall trend is similar to the results with $r \leq R \leq 20r$, except that thicker members are observed in the optimized structure due to the larger R_{max}. The buckling constraints are again satisfied for the cases with $\lambda^* = 1.8, 2.6, 3.7$ (Figs. 15–17) and slightly violated (4.61) for the case with $\lambda^* = 5.0$ (Fig. 18). It is observed that there is clear correlation between the distribution of structural members and of R with large stability margin λ^* (Fig. 18), whereas no clear correlation exists with smaller λ^* (Figs. 15–17). This would be because when the stability margin is large (so it is almost unsatisfiable), the member sizes are primarily

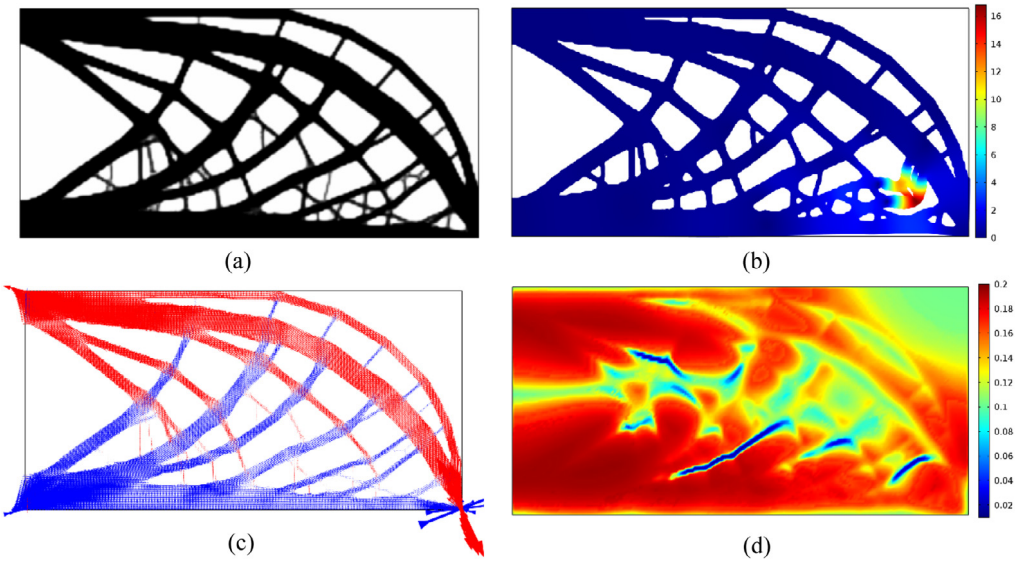

Fig. 14. Functionally-graded lattice cantilever beams with $r \leq R \leq 20r$ and $\lambda^* = 5.0$: (a) Optimized structure (compliance = 0.1928), (b) buckling mode, (c) principal stress, and (d) averaging radius R . (For interpretation of the references to color in this figure legend, the reader is referred to the web version of this article.)

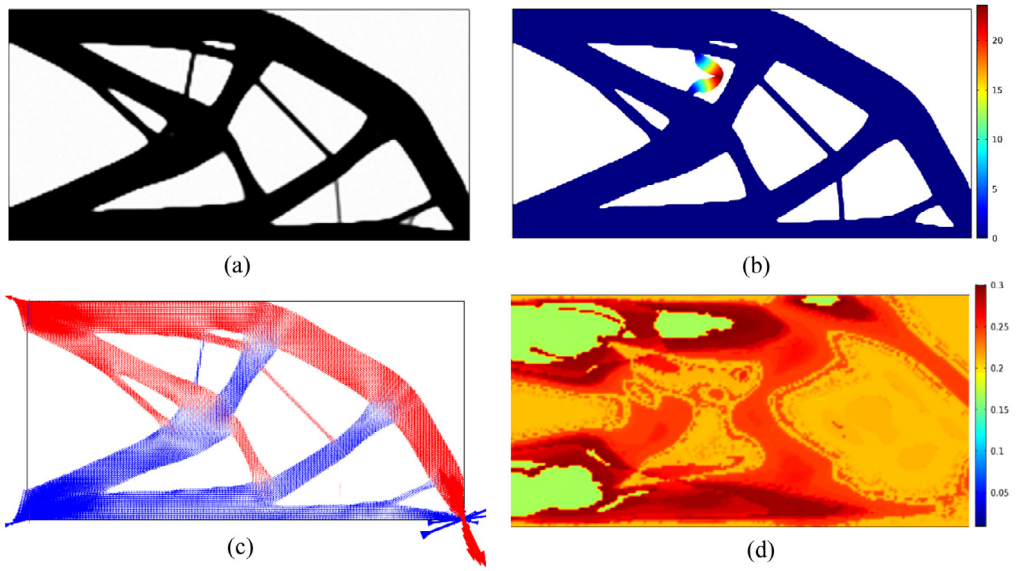

Fig. 15. Functionally-graded lattice cantilever beams with $r \leq R \leq 30r$ and $\lambda^* = 1.8$: (a) Optimized structure (compliance = 0.1857), (b) buckling mode, (c) principal stress, and (d) averaging radius R.

controlled by R to prevent buckling. It is also observed that the optimized structures exhibit many intersections of thick members and slender members. Since both R and density field ϕ (followed with filter radius r to control the minimum length scale) are the design variables, the optimizer could effectively generate such intersections by varying both the radius R in neighborhood and the feature size.

Another example for the illustration of functionally-graded lattice optimization with buckling constraints is shown in Fig. 19. It is a classic column structure with fixed constraint at the bottom and under distributed loads on the top. The design domain is a rectangle area of unit thickness with height $w = 1$ and $h = 2$. The distributed load $d = 1\text{N/m}$ is applied to the middle of top line with $t = 0.96$. The design domain is discretized into 100×200

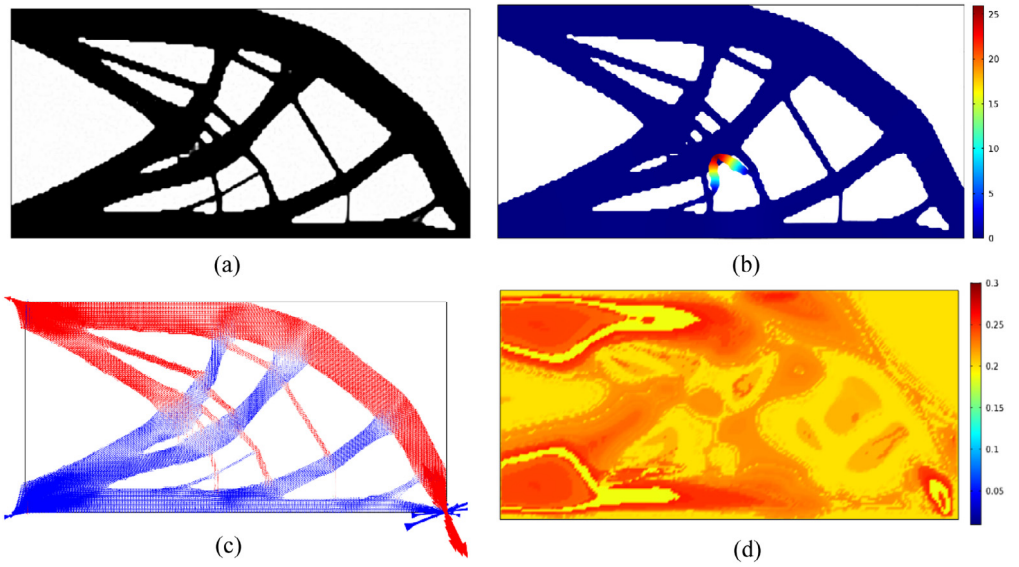

Fig. 16. Functionally-graded lattice cantilever beams with $r \leq R \leq 30r$ and $\lambda^* = 2.6$: (a) Optimized structure (compliance = 0.1871), (b) buckling mode, (c) principal stress, and (d) averaging radius R.

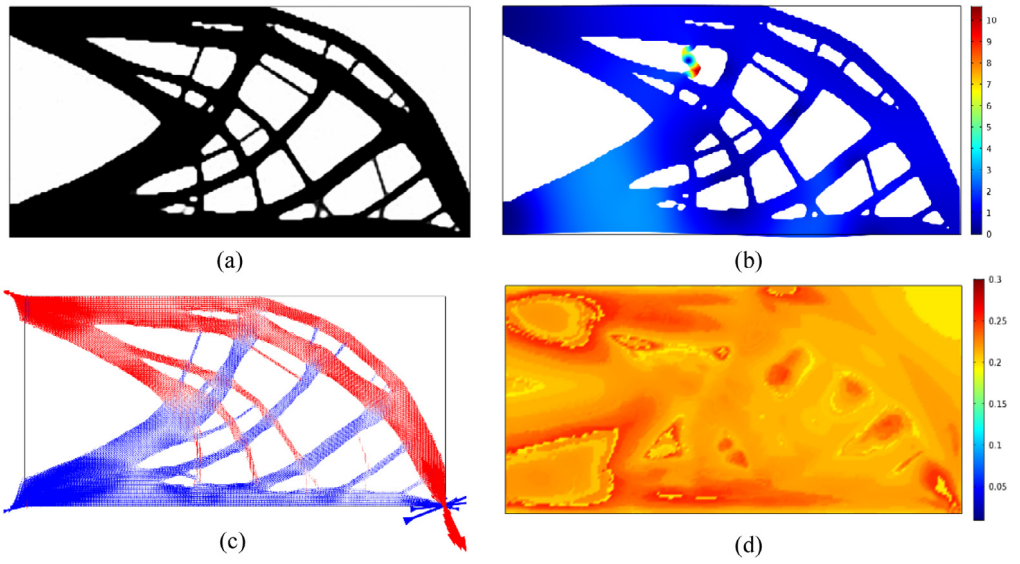

Fig. 17. Functionally-graded lattice cantilever beams with $r \leq R \leq 30r$ and $\lambda^* = 3.7$: (a) Optimized structure (compliance = 0.1872), (b) buckling mode, (c) principal stress, and (d) averaging radius R.

equally-sized square four-node element with Young's modulus $E = 1$ and Poisson's ratio $\nu = 0.3$. The filter radius r is set as the element size, and $V = 0.5$ and $P_l = 0.6$ are used.

The column structure is first optimized without the buckling constraints. Fig. 20 shows the buckling modes (scaling factor = 0.005) and the minimum (normalized) buckling load factor $\overline{\lambda}$ defined in Eq. (20) for the optimized SIMP (Fig. 20(a)) and functionally-graded lattice structures with $r \leq R \leq 10r$ (Fig. 20(b)) and $r \leq R \leq 30r$ (Fig. 20(c)). Similarly to the cantilever example, a larger R_{max} (= $30r$) produces a structure very similar to the one for SIMP with almost the equal compliance. The thin horizontal member that connects the two thick columns appears to improve the structural stability than SIMP, indicated by $\overline{\lambda} = 1.15$. Such co-existence of very thick and very thin members would be very difficult to achieve with a prescribed constant averaging radius R. On the other

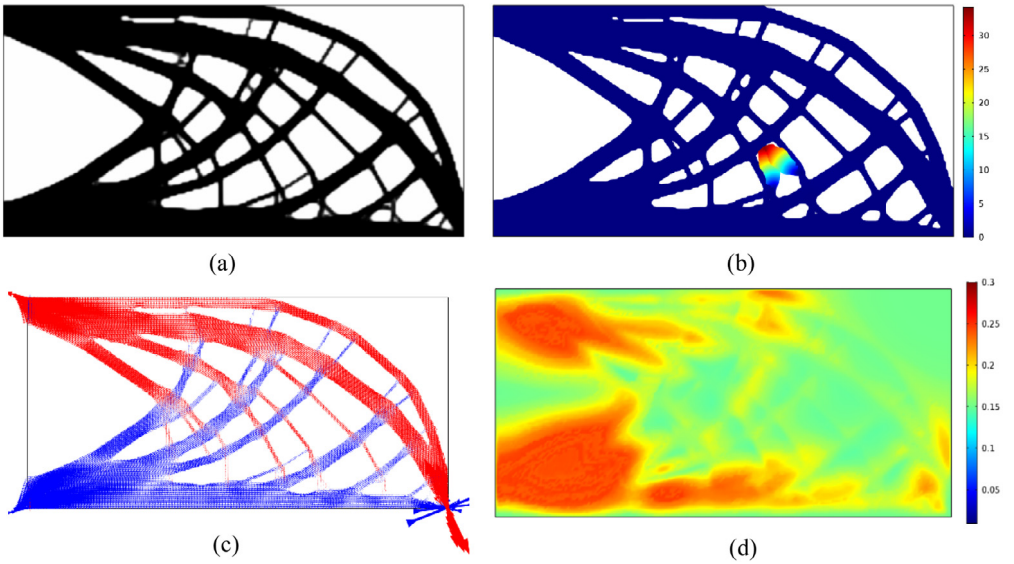

Fig. 18. Functionally-graded lattice cantilever beams with $r \leq R \leq 30r$ and $\lambda^* = 5.0$: (a) Optimized structure (compliance = 0.1925), (b) buckling mode, (c) principal stress, and (d) averaging radius R.

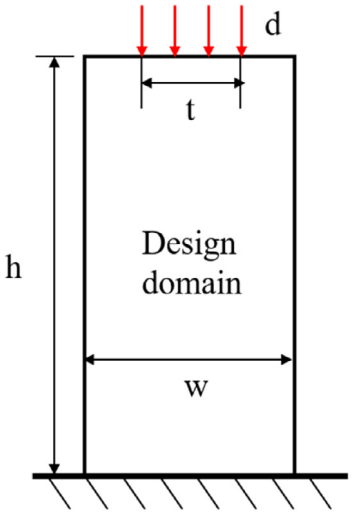

Fig. 19. Design domain and boundary condition for the column structure example.

hand, that the stability of the structure with $R_{max} = 10r$ is worse than the one with $R_{max} = 30r$. Since the members in this structure is primarily under compression, there is a little advantage of enforcing small lattice patterns by a smaller R_{max} for stability improvement, without explicit inclusion of the buckling constraints.

Figs. 21–24 show the optimized structures with $r \leq R \leq 10r$ and different levels of stability margins, $\lambda^* = 1.8, 2.6, 3.7, 5.0$, respectively. In subfigures (b), the scaling factor is set as 0.005. In subfigures (c), tensile stresses are shown in red and compressive stress are shown in blue, with the scale ratio for the magnitude of the tension and compression being 0.01. The buckling constraints are satisfied for the cases with $\lambda^* = 1.8, 2.6, 3.7$ (Figs. 21–23) and slightly violated (4.86) for the case with $\lambda^* = 5.0$ (Fig. 24).

It can be seen in subfigures (a) that the optimized structures exhibit more lattices, especially the thick cross members that connect the vertical columns, as the safety margin λ^*increases. And they do so with little compromise in compliance (*e.g.*, approximately 10% of SIMP for $\lambda^* = 5.0$). The principal stress in subfigures (b) confirms

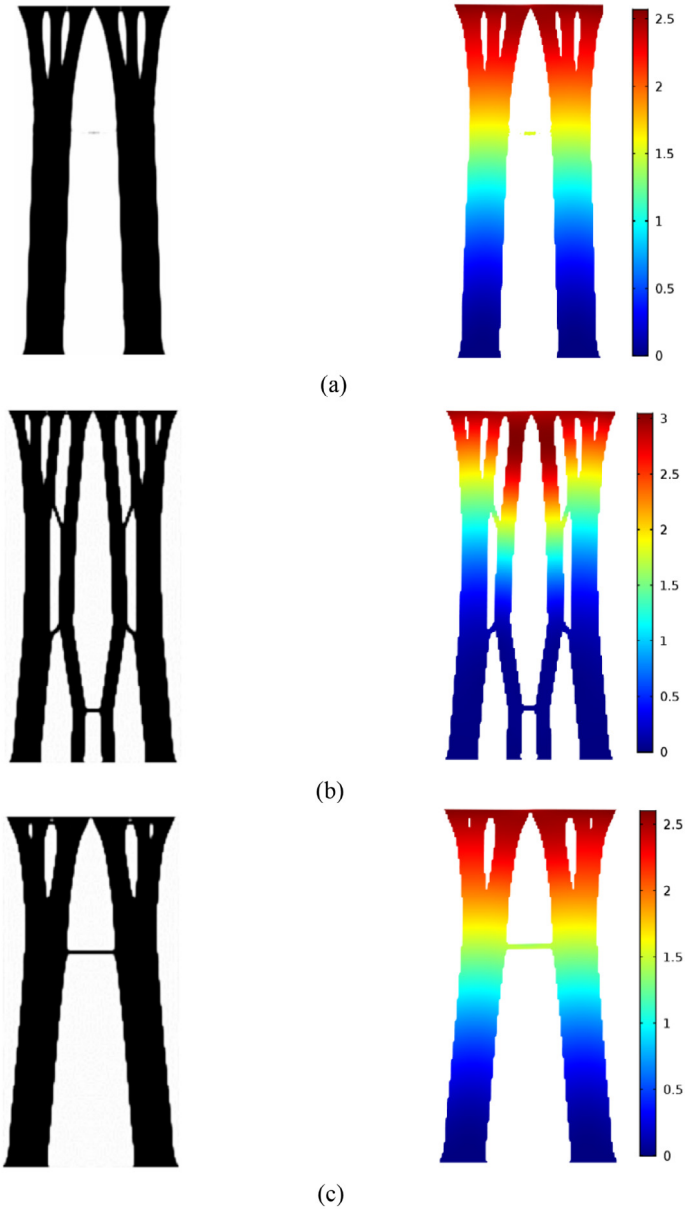

Fig. 20. Optimize structure for SIMP and Variable infill; (a) SIMP, left: optimize structure c = 0.267, right: buckling mode $\overline{\lambda} = 1.0$, (b) variable infill ($r \leq R \leq 10r$), left: optimize structure c = 0.272, right: buckling mode $\overline{\lambda} = 0.59$, (c) Variable infill ($r \leq R \leq 30r$), left: optimize structure c = 0.269, right: buckling mode $\overline{\lambda} = 1.15$.

the vertical columns are under compression, whose stability against local buckling would improve with the cross members connecting them along their length. Similar to the cantilever example, subfigures (d) indicates the optimized structures utilize smaller averaging radius that would create more lattices as the level of stability margin increases, with a clear correlation between the member sizes and the averaging radius.

Figs. 25–28 show the optimized structures with $r \leq R \leq 30r$ and different levels of stability margins, $\lambda^* = 1.8, 2.6, 3.7, 5.0$, respectively. The buckling constraints are again satisfied for the cases with $\lambda^* = 1.8, 2.6, 3.7$ (Figs. 25–27) and slightly violated (4.92) for the case with $\lambda^* = 5.0$ (Fig. 28). The optimized structures are overall similar to the one by SIMP with thick columns (thanks to the larger R_{max}), except for the $\lambda^* = 5.0$ case where the optimizer could not satisfy the buckling constraint even with 10% compromise in compliance.

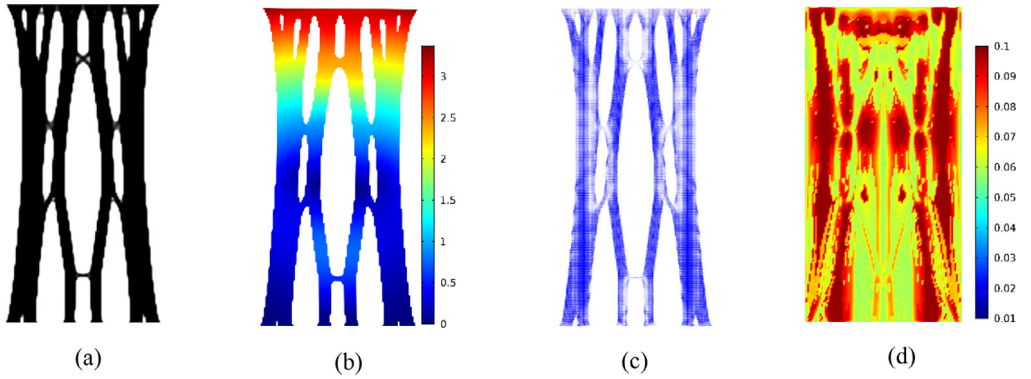

Fig. 21. Functionally-graded lattice column structure with $r \leq R \leq 10r$ and $\lambda^* = 1.8$: (a) Optimized structure (compliance = 0.271), (b) buckling mode, (c) principal stress, and (d) averaging radius R . (For interpretation of the references to color in this figure legend, the reader is referred to the web version of this article.)

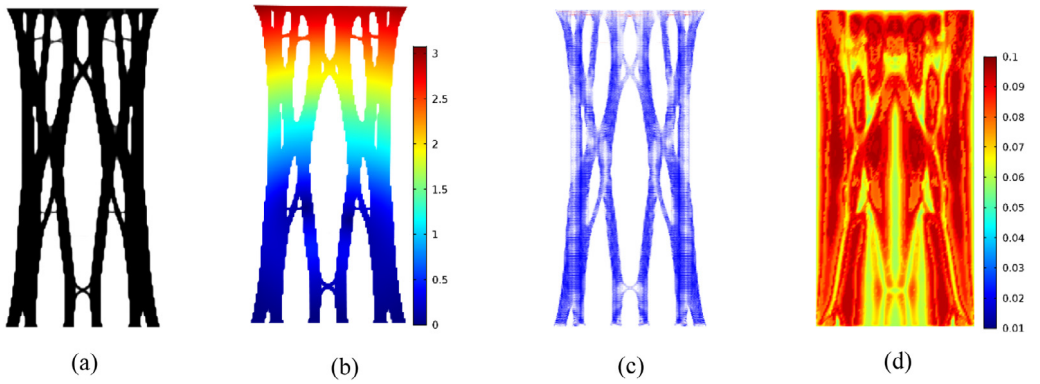

Fig. 22. Functionally-graded lattice column structure with $r \leq R \leq 10r$ and $\lambda^* = 2.6$: (a) Optimized structure (compliance = 0.275), (b) buckling mode, (c) principal stress, and (d) averaging radius R . (For interpretation of the references to color in this figure legend, the reader is referred to the web version of this article.)

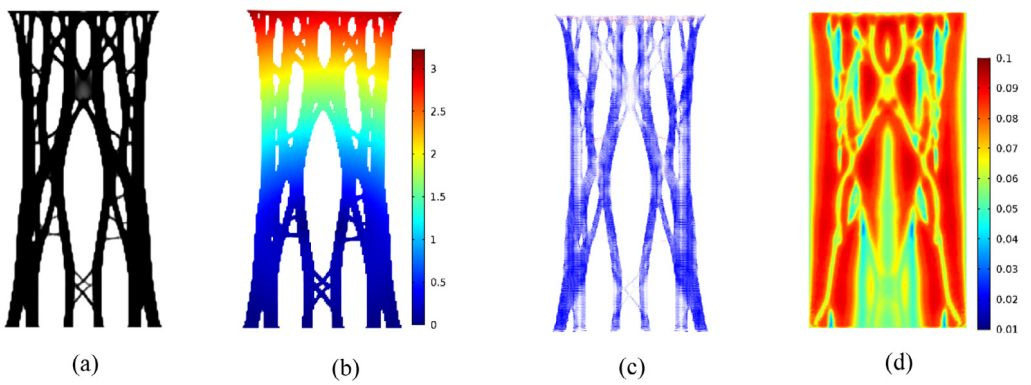

Fig. 23. Functionally-graded lattice column structure with $r \leq R \leq 10r$ and $\lambda^* = 3.7$: (a) Optimized structure (compliance = 0.286), (b) buckling mode, (c) principal stress, and (d) averaging radius R . (For interpretation of the references to color in this figure legend, the reader is referred to the web version of this article.)

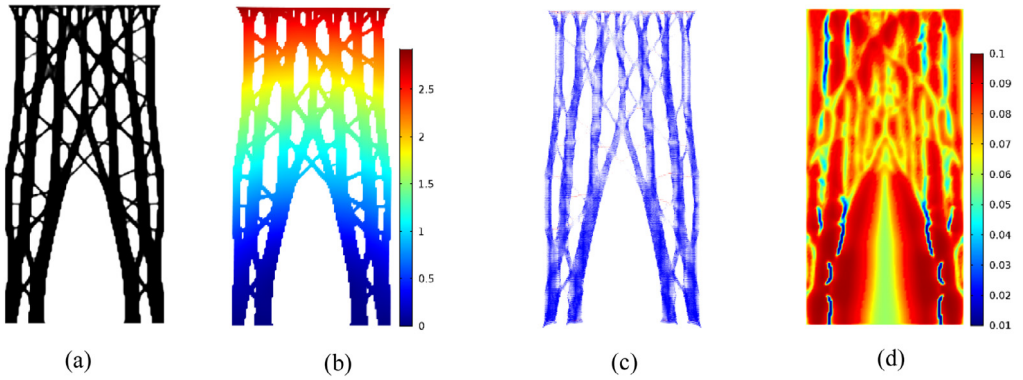

Fig. 24. Functionally-graded lattice column structure with $r \leq R \leq 10r$ and $\lambda^* = 5.0$: (a) Optimized structure (compliance = 0.298), (b) buckling mode, (c) principal stress, and (d) averaging radius R . (For interpretation of the references to color in this figure legend, the reader is referred to the web version of this article.)

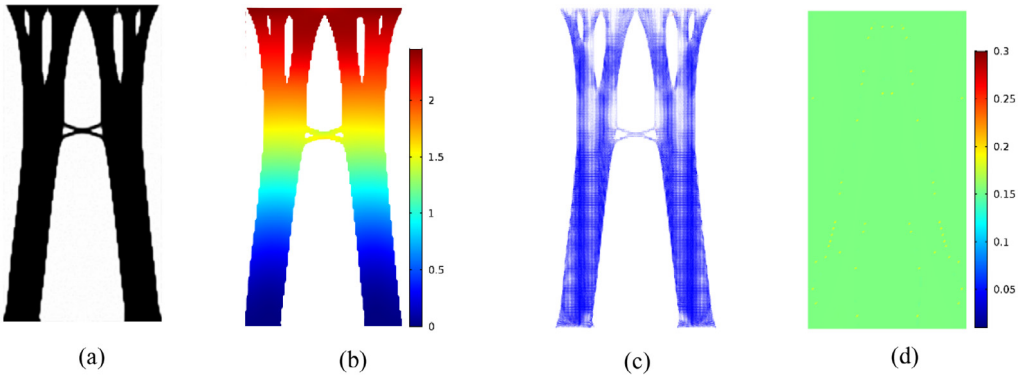

Fig. 25. Functionally-graded lattice column structure with $r \leq R \leq 30r$ and $\lambda^* = 1.8$: (a) Optimized structure (compliance = 0.274), (b) buckling mode, (c) principal stress, and (d) averaging radius R.

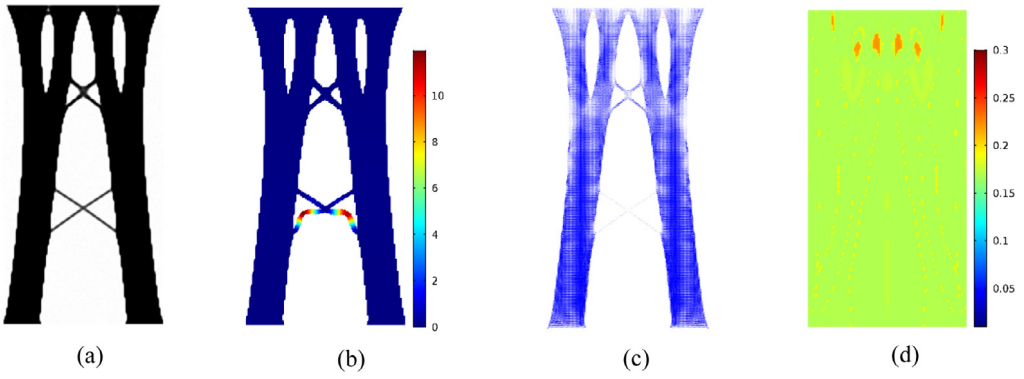

Fig. 26. Functionally-graded lattice column structure with $r \leq R \leq 30r$ and $\lambda^* = 2.6$: (a) Optimized structure (compliance = 0.277), (b) buckling mode, (c) principal stress, and (d) averaging radius R.

5. Conclusion

This paper presented a topology optimization method for structures with functionally-graded lattices with buckling constraints, which minimizes compliance while ensuring a prescribed level of structural stability against buckling failures. To realize topologically-optimized structures filled with functionally-graded lattices, Helmholtz

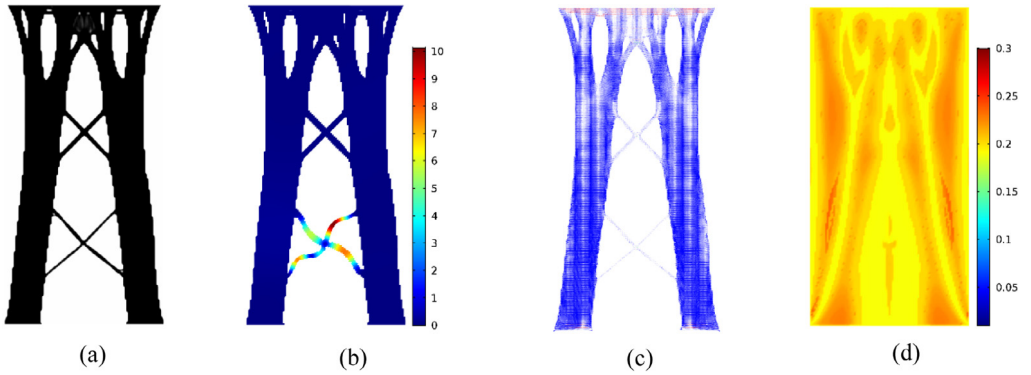

Fig. 27. Functionally-graded lattice column structure with $r \leq R \leq 30r$ and $\lambda^* = 3.7$: (a) Optimized structure (compliance = 0.278), (b) buckling mode, (c) principal stress, and (d) averaging radius R.

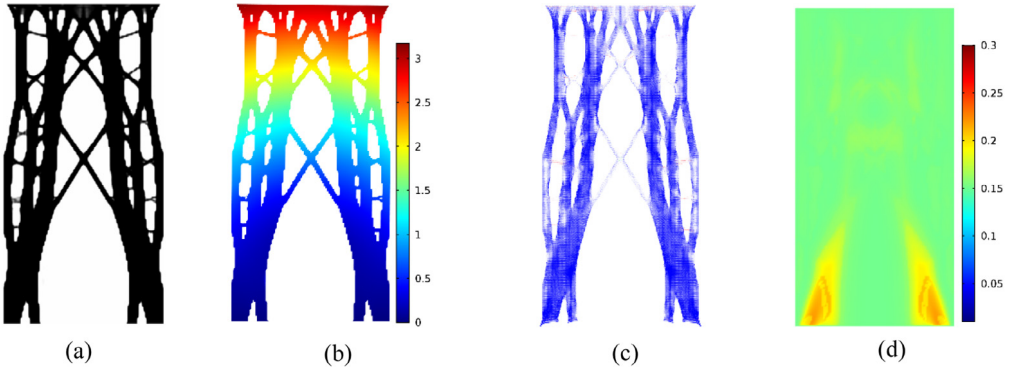

Fig. 28. Functionally-graded lattice column structure with $r \leq R \leq 30r$ and $\lambda^* = 5.0$: (a) Optimized structure (compliance = 0.294), (b) buckling mode, (c) principal stress, and (d) averaging radius R.

PDE-filter with a variable radius is applied on the density field in Solid Isotropic Material with Penalization (SIMP) method. Buckling load factors based on the linear buckling analysis is employed as buckling constraints. Numerical examples show that proposed method can generate stiff structures comparable to the ones by the SIMP, with smoothly connected, functionally-graded lattices that improve the structural stability by avoiding long, slender features under compression.

As with most topology optimization schemes, the proposed method is prone to get trapped in local minima as evidenced by asymmetric designs and apparent drop-outs or misalignments of secondary lattice members. Overall, however, the reported results appear to suffer from this problem less than many others, as they exhibit compliance values comparable to equivalent structures obtained by the SIMP method.

The paper presented only 2D examples. While the proposed formulation is not limited to 2D, the large computational cost of buckling analysis remains as a challenge for 3D extension. Also, the paper considered only the linear buckling analysis. The incorporation of nonlinear buckling and post-buckling are also left as the future work.

Acknowledgments

This work has been conducted during the first and third authors' visit at the University of Michigan for their sabbatical. The financial supports were provided by National Natural Science Foundation of China under Grant No. 51605495, Natural Science Foundation of Hunan Province, China under Grant No. 2018JJ3663, and International Postdoctoral Exchange Fellowship, China Program Grant NO. 2017[59] for the first author. These sources of supports are gratefully acknowledged.

References

[1] X. Zheng, H. Lee, T.H. Weisgraber, M. Shusteff, J. DeOtte, E.B. Duoss, J.D. Kuntz, M.M. Biener, Q. Ge, J.A. Jackson, S.O. Kucheyev, N.X. Fang, C.M. Spadaccini, Ltralight, ultrastiff mechanical metamaterials, Science 344 (6190) (2014) 1373–1377.

[2] D. Fujii, B.C. Chen, N. Kikuchi, Composite material design of two-dimensional structures using the homogenization design method, Internat. J. Numer. Methods Engrg. 50 (9) (2001) 2031–2051.

[3] D. Jang, L.R. Meza, F. Greer, J.R. Greer, Fabrication and deformation of three-dimensional hollow ceramic nanostructures, Nature Mater. 12 (10) (2013) 893–898.

[4] J.H. Lee, L. Wang, S. Kooi, M.C. Boyce, E.L. Thomas, Enhanced energy dissipation in periodic epoxy nanoframes, Nano Lett. 10 (7) (2010) 2592–2597.

[5] A.G. Evans, M.Y. He, V.S. Deshpande, J.W. Deshpande, A.J. Hutchinson, W.B. Jacobsen, Carter, Concepts for enhanced energy absorption using hollow micro-lattices, Int. J. Impact Eng. 37 (9) (2010) 947–959.

[6] R. Lakes, Foam structures with a negative Poisson's ratio, Science 235 (4792) (1987) 1038–1040.

[7] E. Andreassen, B.S. Lazarov, O. Sigmund, Design of manufacturable 3D extremal elastic microstructure, Mech. Mater. 69 (1) (2014) 1–10.

[8] A. Clausen, F. Wang, J.S. Jensen, O. Sigmund, J.A. Lewis, Topology optimized architectures with programmable Poisson's ratio over large deformations, Adv. Mater. 27 (37) (2015) 5523–5527.

[9] O. Sardan, D.H. Petersen, K. Mølhave, O. Sigmund, P. Boggild, Topology optimized electrothermal polysilicon microgrippers, Microelectron. Eng. 85 (5–6) (2008) 1096–1099.

[10] A. Takezawa, M. Kobashi, M. Kitamura, Porous composite with negative thermal expansion obtained by photopolymer additive manufacturing, APL Mater. 3 (7) (2015) 076103.

[11] Y. Li, Y. Chen, T. Li, S. Cao, L. Wang, Hoberman-sphere-inspired lattice metamaterials with tunable negative thermal expansion, Compos. Struct. 189 (2018) 586–597.

[12] G.H. Yoon, J.S. Jensen, O. Sigmund, Topology optimization of acoustic–structure interaction problems using a mixed finite element formulation, Internat. J. Numer. Methods Engrg. 70 (9) (2007) 1049–1075.

[13] F. Chevillotte, C. Perrot, Effect of the three-dimensional microstructure on the sound absorption of foams: A parametric study, J. Acoust. Soc. Am. 142 (2) (2017) 1130–1140.

[14] Y. Noguchi, T. Yamada, K. Izui, S. Nishiwaki, Topology optimization for hyperbolic acoustic metamaterials using a high-frequency homogenization method, Comput. Methods Appl. Mech. Eng. 335 (2018) 419–471.

[15] T.A. Schaedler, W.B. Carter, Architected cellular materials, Annu. Rev. Mater. Res. 46 (1) (2016) 187–210.

[16] G. Dong, Y. Tang, Y. Zhao, A survey of modeling of lattice structures fabricated by additive manufacturing, J. Mech. Des. 139 (10) (2017) 100906-1–13.

[17] M.P. Bendsoe, N. Kikuchi, Generating optimal topologies in structural design using a homogenization method, Comput. Methods Appl. Mech. Eng. 71 (2) (1988) 197–224.

[18] M.P. Bendsoe, O. Sigmund, Material interpolation schemes in topology optimization, Arch. Appl. Mech. 69 (9–10) (1999) 635–654.

[19] C. Liu, Z. Du, W. Zhang, Y. Zhu, X. Guo, Additive manufacturing oriented design of graded lattice structures through explicit topology optimization, J. Appl. Mech. 84 (8) (2017) 081008-1-12.

[20] J. Wu, N. Aage, R. Westermann, O. Sigmund, Infill optimization for additive manufacturing - approaching bone-like porous structures, IEEE Trans. Vis. Comput. Graphics 24 (2) (2016) 1127–1140.

[21] J. Wu, A. Clausen, O. Sigmund, Minimum compliance topology optimization of shell-infill composites for additive manufacturing, Comput. Methods Appl. Mech. Engrg. 326 (2017) 358–375.

[22] E. Träff, O. Sigmund, J. Groen, Simple single-scale microstructures based on optimal rank-3 laminates, 2018, ArXiv preprint, arXiv: 1809.03942.

[23] P.G. Coelho, J.B. Cardoso, P.R. Fernandes, H.C. Rodrigues, Parallel computing techniques applied to the simultaneous design of structure and material, Adv. Eng. Softw. 42 (5) (2011) 219–227.

[24] W. Chen, L. Tong, S. Liu, Concurrent topology design of structure and material using a two-scale topology optimization, Comput. Struct. 178 (2017) 119–128.

[25] Y. Wang, H. Xu, D. Pasini, Multiscale isogeometric topology optimization for lattice materials, Comput. Methods Appl. Mech. Engrg. 316 (2017) 568–585.

[26] W. Chuang, Z.J. Hong, Z.W. Hong, S. Ying, K. Jie, Concurrent topology optimization design of structures and non-uniform parameterized lattice microstructures, Struct. Multidiscip. Optim. 58 (1) (2018) 35–50.

[27] A. Panesar, M. Abdi, D. Hickman, I. Ashcroft, Strategies for functionally graded lattice structures derived using topology optimisation for additive manufacturing, Additive Manuf. 19 (2018) 81–94.

[28] A. Radman, X. Huang, Y.M. Xie, Topology optimization of functionally graded cellular materials, J. Mater. Sci. 48 (4) (2013) 1503–1510.

[29] S. Daynes, S. Feih, W.F. Lu, J. Wei, Optimisation of functionally graded lattice structures using isostatic lines, Mater. Des. 127 (2017) 215–223.

[30] H. Li, Z. Luo, L. Gao, P. Walker, Topology optimization for functionally graded cellular composites with metamaterials by level sets, Comput. Methods Appl. Mech. Engrg. 328 (2017) 340–364.

[31] J. Deng, W. Chen, Concurrent topology optimization of multiscale structures with multiple porous materials under random field loading uncertainty, Struct. Multidiscip. Optim. 56 (1) (2017) 1–19.

[32] L. Xu, G. Cheng, Two-scale concurrent topology optimization with multiple micro materials based on principal stress orientation, Struct. Multidiscip. Optim. 57 (5) (2018) 2093–2107.

[33] Y. Wang, F. Chen, M.Y. Wang, Concurrent design with connectable graded microstructures, Comput. Methods Appl. Mech. Engrg. 317 (2017) 84–101.
[34] S. Nishi, K. Terada, J. Kato, S. Nishiwaki, K. Izui, Two-scale topology optimization for composite plates with in-plane periodicity, Internat. J. Numer. Methods Engrg. 113 (8) (2017) 1164–1188.
[35] F. Campagna, A.R. Diaz, Optimization of lattice infill distribution in additive manufacturing, Int. Design Eng. Tech. Conf. Comput. Inform. Eng. Conf. (2A) (2017) V02AT03A028.
[36] Z. Du, H.A. Kim, Multiscale design considering microstructure connectivity, in: 2018 AIAA/ASCE/AHS/ASC Structures, Structural Dynamics, and Materials Conference, 2018, pp. 1385.
[37] O. Pantz, K. Trabelsi, A post-treatment of the homogenization method for shape optimization, SIAM J. Control Optim. 47 (3) (2008) 1380–1398.
[38] J.P. Groen, O. Sigmund, Homogenization-based topology optimization for high-resolution manufacturable microstructures, Internat. J. Numer. Methods Engrg. 113 (8) (2017) 1148–1163.
[39] G. Allaire, P. Geoffroy-Donders, O. Pantz, Topology Optimization of Modulated and Oriented Periodic Microstructures By the Homogenization Method, 2018,.
[40] J. Panetta, Q. Zhou, L. Malomo, N. Pietroni, P. Cignoni, D. Zorin, Elastic textures for additive fabrication, ACM Trans. Graph. 34 (4) (2015) 135:1–135:12.
[41] B. Zhu, M. Skouras, D. Chen, W. Matusik, Two-scale topology optimization with microstructures, ACM Trans. Graph. 36 (5) (2017) 164.
[42] N. Takano, M. Zako, Integrated design of graded microstructures of heterogeneous materials, Arch. Appl. Mech. 70 (8–9) (2000) 585–596.
[43] L. Xia, P. Breitkopf, Multiscale structural topology optimization with an approximate constitutive model for local material microstructure, Comput. Methods Appl. Mech. Engrg. 286 (2015) 147–167.
[44] N.S. Khot, V.B. Venkayya, L. Berke, Optimum structural design with stability constraints, Internat. J. Numer. Methods Engrg. 10 (5) (1976) 1097–1114.
[45] M.M. Neves, H.C. Rodrigues, J.M. Guedes, Generalized topology design of structures with a buckling load criterion, Struct. Optim. 10 (2) (1995) 71–78.
[46] Q. Luo, L. Tong, Structural topology optimization for maximum linear buckling loads by using a moving iso-surface threshold method, Struct. Multidiscip. Optim. 52 (1) (2015) 71–90.
[47] X. Gao, H. Ma, Topology optimization of continuum structures under buckling constraints, Comput. Struct. 157 (2015) 142–152.
[48] P.D. Dunning, E. Ovtchinnikov, J. Scott, H.A. Kim, Level-set topology optimization with many linear buckling constraints using an efficient and robust eigensolver, Internat. J. Numer. Methods Engrg. 107 (12) (2016) 1029–1053.
[49] G. Cheng, L. Xu, Two-scale topology design optimization of stiffened or porous plate subject to out-of-plane buckling constraint, Struct. Multidiscip. Optim. 54 (5) (2016) 1283–1296.
[50] W. Zhang, Y. Liu, Z. Du, Y. Zhu, X. Guo, A moving morphable component (MMC)-based topology optimization approach for rib-stiffened structures considering buckling constraints, J. Mech. Des. 140 (11) (2018) 111404–111404-12.
[51] C. Wu, J. Fang, Q. Li, Multi-material topology optimization for thermal buckling criteria, Comput. Methods Appl. Mech. Engrg. 346 (2019) 1136–1155.
[52] C.R. Thomsen, F. Wang, O. Sigmund, Buckling strength topology optimization of 2d periodic materials based on linearized bifurcation analysis, Comput. Methods Appl. Mech. Eng. 339 (2018) 115–136.
[53] F. Ferrari, O. Sigmund, Revisiting topology optimization with buckling constraints, 2018, ArXiv preprint, arXiv:1809.05300.
[54] B.S. Lazarov, O. Sigmund, Filters in topology optimization based on Helmholtz-type differential equations, Internat. J. Numer. Methods Engrg. 86 (6) (2011) 765–781.
[55] A. Kawamoto, T. Matsumori, S. Yamasaki, T. Nomura, T. Kondoh, S. Nishiwaki, Heaviside projection based topology optimization by a PDE-filtered scalar function, Struct. Multidiscip. Optim. 44 (1) (2011) 19–24.
[56] R. De Borst, M.A. Crisfield, J.J. Remmers, C.V. Verhoosel, Nonlinear Finite Element Analysis of Solids and Structures, second ed., John Wiley & Sons, 2012.
[57] H.C. Rodrigues, J.M. Guedes, M.P. Bendsoe, Necessary conditions for optimal design of structures with a nonsmooth eigenvalue based criterion, Struct. Optim. 9 (1) (1995) 52–56.
[58] J. Gravesen, A. Evgrafov, D.M. Nguyen, On the sensitivities of multiple eigenvalues, Struct. Multidiscip. Optim. 44 (4) (2011) 583–587.
[59] K. Svanberg, The method of moving asymptotes - A new method for structural optimization, Internat. J. Numer. Methods Engrg. 24 (2) (1987) 359–373.